Thomas Kroißenbrunner, BSc

Quasi-resonant Amplification in a Changing Climate

MASTER'S THESIS

to achieve the university degree of

Master of Science

Master's degree programme: Physics

submitted to

Graz University of Technology

Supervisor

Douglas Maraun, Assoz. Prof. Dr.

Co-Supervisor

Albert Osso, Ass.-Prof. PhD

Graz, September 2020

AFFIDAVIT

I declare that I have authored this thesis independently, that I have not used other than the declared sources/resources, and that I have explicitly indicated all material which has been quoted either literally or by content from the sources used. The text document uploaded to TUGRAZonline is identical to the present master's thesis.

Date, Signature

Abstract

Based on purely thermodynamical considerations, heat waves are expected to increase in frequency and intensity in a changing climate. Impacts on the dynamics that produce heat waves are however less understood. Recent research has emerged regarding the climate change influence on a specific heat wave producing mechanism, the so-called Quasi-resonant Amplification (QRA). Mann et al. (2017) used characteristics in the surface temperature field during QRA events to define a fingerprint in order to draw conclusions about trends in QRA-favouring conditions. In this thesis, this research is extended to take a fuller picture of the atmosphere during these events into account. Specifically, internal variability of QRA events and summer climatologies (June, July and August mean) was assessed, showing that QRA variability lies within one standard deviation of the summer means. Additionally similar fingerprints as the surface fingerprint were calculated for upper levels of the atmosphere that revealed a vertical structure in addition to the meridional structure found by Mann et al. (2017). Furthermore, these fingerprints were projected onto yearly summer temperature fields for historical (observational, reanalysis and modelling) and simulated future data. The results show a large internal as well as across-models variability of the regression coefficients, for all pressure levels taken into consideration. Finally, the relative contribution of individual atmospheric layers to the thermally driven jet were analysed with the thermal wind equation, revealing no significant trends in the emergence of a certain layer with highest contribution to the thermally driven jet since 1979.

Kurzfassung

In einem sich erwärmenden Klima wird aufgrund von thermodynamischen Überlegungen erwartet das Hitzewellen an Stärke und Häufigkeit zunehmen. Veränderung der grundlegenden Dynamik von Hitzewellen sind allerdings weniger verstanden. Quasi-resonant Amplification (QRA) ist eine Theorie die einen Mechanismus für die Entstehung von Hitzeperioden beschreibt. Mann et al. (2017) benutzten Charakteristika im Oberflächentemperaturfeld während QRA-Events um mithilfe eines Fingerabdrucks Aussagen über Trends in QRA-begünstigenden Bedingungen zu treffen. Das Ziel der vorliegenden Arbeit ist es ein volleres Bild der Atmosphäre während dieser QRA-Events zu beschreiben. Interne Variabilität von QRA-Events und Sommer Klimatologien (Mittelwert über Juni, Juli und August) wurde untersucht. Es kann gezeigt werden dass die QRA-Variabilität innerhalb einer Standardabweichung der Sommer Mittelwerte liegt. Zusätlich wurden Fingerabdrücke auch für obere Atmosphärenschichten berechnet, die eine vertikale Struktur zusätzlich zu der von Mann et al. (2017) gefundenen meridionalen Struktur zeigen. Projektionen dieser Fingerabdrücke auf jährliche Sommer Temperaturklimatologien für historische (Beobachtungs-, Reanalysis- und Simulationsdaten) und simulierte Zukunftsszenarien zeigt eine hohe interne und Klimamodell übergreifende Variabilität. Im letzten Teil werden die relativen Beiträge individueller Atmosphärenschichten zum Temperaturgetriebenen Teil des Jets, mithilfe der Thermal-Wind Gleichung, untersucht.

Danksagung

Den größte Dank möchte ich an meine Eltern, Daniela und Werner, richten. Sie haben mich im Laufe meines Studiums nicht nur finanziell unterstützt, sondern mir darüber hinaus auch ausreichend Freiraum für meine persönliche Entwicklung zur Verfügung gestellt und mir stets Vertrauen geschenkt. Danke auch an meine Freunde, ob auf der Universität oder extern, die mich immer herausforderten und motivierten mein Potential auszuschöpfen, aber andererseits auch immer für mich da waren wenn mir das einmal nicht gelang.
Des Weiteren möchte ich mich bei Assoz.Prof. Dr. Douglas Maraun und Ass.-Prof. PhD Albert Osso bedanken, die stets für anregende Diskussionen bereit waren und mir oft Mut machten, und bei allen Kollegen der ReLoClim Arbeitsgruppe, die mich angenehm aufnahmen und mir stets viel beibringen.

Contents

List of Figures

List of Tables

1 Introduction

Heat waves can cause strong socio-economic impacts through heat-related deaths, forest fires, droughts and crop losses. Examples for recent, well investigated summer extremes are the European heat wave in 2003 (De Bono et al. 2004), the Russian heat wave in 2010 with more than 55,000 causalities (Grumm 2011) and the United States heat wave in 2011 (Peterson et al. 2012). Due to the potentially hazardous nature of heat waves, a key understanding of the processes that are responsible for them is much needed. Taking into account the severity of recent extremes as well as their increase in frequency (Kornhuber et al. 2019), it is important to understand how climate change affects heat waves and their underlying drivers. From purely thermodynamical considerations, heat waves are expected to increase in frequency and intensity (Schär et al. 2004). However, the impact of climate change on their dynamical behaviour remains much more elusive, owing to the complexity of all processes at play.

Heat waves are often associated with persistent large scale-circulation patterns, local feedbacks as well as land and atmosphere coupling (Fischer et al. 2007). Highly complex interactions between the different potential drivers for heat waves can make it difficult to find one coherent theory to explain them. However, one such theory that has emerged only in recent years as a possible explanation is called Quasi-Resonant Amplification (QRA) (Petoukhov et al. 2013, Kornhuber et al. 2016). QRA is an atmospheric phenomena involving quasi-stationary forced planetary scale and free travelling synoptic scale Rossby waves (Hoskins et al. 1977, Hoskins & Karoly 1981, Petoukhov et al. 2013). When certain dynamical conditions occur, free travelling and stationary Rossby waves can resonate to cause quasi-stationary high amplitude Rossby waves, which can be associated with heat waves or droughts (Petoukhov et al. 2013). The dynamics of QRA are hypothesized to be influenced by climate change.

The Arctic is warming more than twice as fast as the global average (Screen & Simmonds 2010). This Arctic amplification (AA) is thought to cause a weakening of the meridional surface temperature gradient, consequently reducing the strength of the jet stream via the thermal wind equation, favouring the occurrence of QRA events (Kornhuber et al. 2016, Mann et al. 2017). Arguing that climate models do not model dynamics as well as thermodynamics, Mann et al. (2017) (M17) used anomalous zonal mean surface temperature fields during QRA events to define a fingerprint, which has been used to investigate the influence of climate change on QRA (Mann et al. 2018) (M18). The results show a likely increase of QRA events in this century by 50%. However there is a large spread among climate models, showing changes of opposite signs. One of the major goals of this thesis is to further analyse and extend the concept of the QRA fingerprint, as well as test its assumptions.

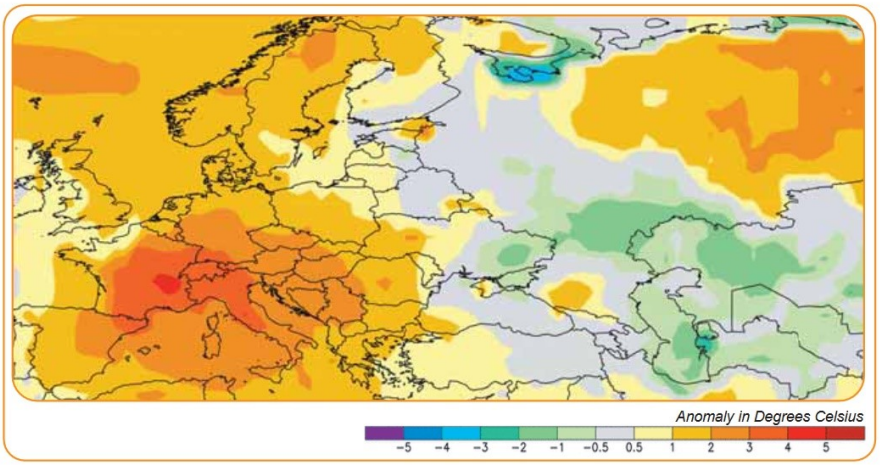

Figure 1.1: Anomalous temperature for the European heat wave of 2003. Climatological base period is 1988-2003. A composite of in-situ and satellite data has been used (NDC/NOAA). Source: De Bono et al. (2004).

European heat wave of 2003

In 2003, Europe suffered a record breaking heat wave that resulted in almost 15,000 deaths in France alone and additionally 4,000 in the United Kingdom and Portugal (Koppe et al. 2004), with financial losses estimated to be over 13 billion Euros (De Bono et al. 2004). The heat wave started in July and lasted until August, with temperatures being above long-time averages for a duration of 20 days. A big portion of the continent was affected by anomalously high temperatures, as can be seen in Fig 1.1. Strong anticyclonic patterns persisted from May to August, favouring transport of hot, dry air to Europe (Black et al. 2004).
Taking thermodynamical considerations of climate change into account (Schär et al. 2004), such a record breaking event as the European heat wave of 2003 is still highly unlikely (Luterbacher et al. 2004). A different independent mechanism has to be at work to allow for heat waves such as this one.
Petoukhov et al. (2013) analysed meteorological conditions and found high-amplitude contributions of stationary waves with zonal wave numbers $m = 6, 7$ and 8 for several recent summer heat waves, including the European heat wave of 2003. This provides evidence for QRA to be a main mechanism behind the event. A double-spiked profile of the monthly and zonally averaged zonal wind at 300 hPa is often associated to be a precursor to QRA events (Mann et al. 2017, 2018, Petoukhov et al. 2013). Fig. 1.2 clearly exhibits this double-spiked jet profile for July and August of 2003, further supporting the QRA theory.

European heat wave of 2018

A more recent example for a devastating heat wave was the European heat wave of 2018 that featured distinct spatio-temporal patterns (Bastos et al. 2020). In June, the British Isles suffered the highest temperatures, whereas in July, Scandinavia and central Europe, and in August, south-

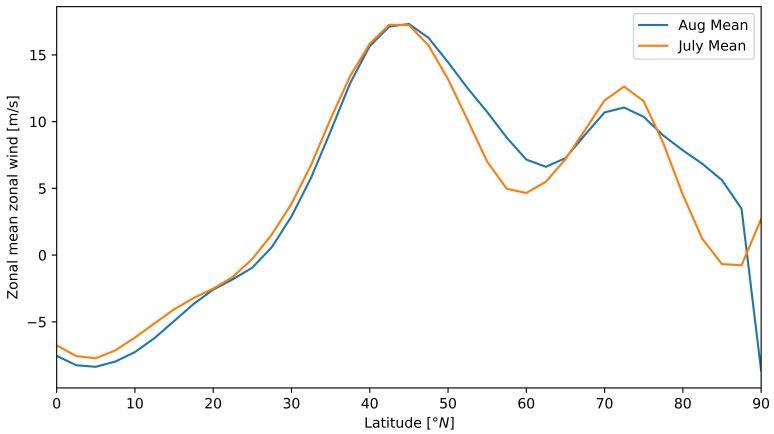

Figure 1.2: July and August means of zonally averaged 300 hPa zonal wind in 2003.

western Europe were affected most by the temperature extremes (Barriopedro et al. 2020). Over central and northern Europe, an extreme drought led to crop losses and major economic costs. In Fig. 1.3 the soil moisture (SM) anomaly is shown, clearly indicating the areas affected by the drought.
Kornhuber et al. (2019) analysed the mid-latitude circulation and found a circumglobal wave number 7 teleconnection pattern in the northern hemisphere, that was not only responsible for the European heat wave, but also heat waves in North America and the Caspian sea region. They additionally show that the frequency and persistence of this teleconnection pattern has increased in recent years.
Vogel et al. (2019) analysed Earth System Model simulations and found that it is *virtually certain* (using the calibrated language of the Intergovernmental Panel on Climate Change) that this concurrent Northern Hemisphere extreme events would not have occurred without anthropogenic influence on the climate.

Overview

This thesis is aimed at investigating the concept of the QRA fingerprint as defined by Mann et al. (2017), and extending it to various pressure levels in order to take into account a fuller range of possible climate change influences. In Chapter 2 the underlying concepts and drivers of heat waves are discussed. In particular, Section 2.2 will be dedicated to the theory of QRA. The influence of climate change on heat waves through thermodynamical principles will be discussed in Section 3.1, theories for possible contributions to changes in mid-latitude dynamics are given in Section 3.2. The data that was used and methods for QRA detection are given in Chapter 4, along with the mathematical formalism of QRA and relevant equations for the analyses done in this thesis (Section 4.2). Chapter 5 is dedicated to analysing internal variability of JJA climatologies as well as QRA events (Section 5.1), looking into the vertical structure of

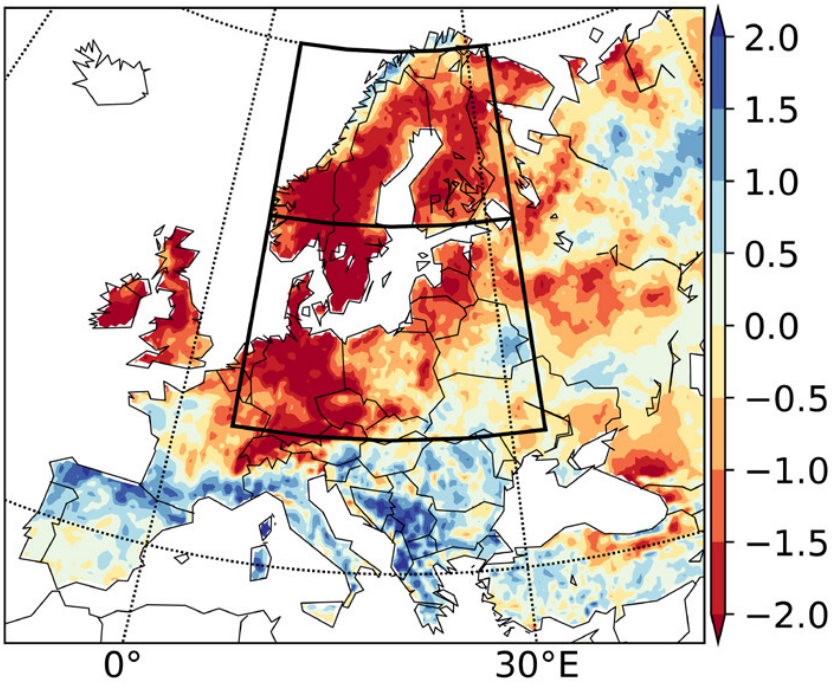

Figure 1.3: Soil moisture (SM) anomaly in Europe from ERA5 fields of summer (JJA) 2018. Source: Bastos et al. (2020).

the fingerprint (Section 5.2) as well as projecting the calculated fingerprint onto yearly zonal mean JJA temperature fields to see if the relationship has changed (Section 5.3). In Chapter 6, the wind shear was calculated using the thermal wind equation for different layers of the atmosphere and compared to the observed wind shear. Finally, in Chapter 7 the presented results are summarized and further ideas for research are presented.

2 Heat wave mechanisms

Large, quasi-stationary meanders in the jet stream cause persistent anomalous weather that can be extreme, and further intensify due to various feedbacks mechanisms. Depending on season, the resulting weather patterns are either heat or cold waves. In this Chapter, different types of these persistent patterns and their sustaining mechanisms are discussed, as well as feedbacks that further intensify the weather to extremes. In the last Section, the theory of quasi-resonant amplification of Rossby waves is demonstrated as a possible explanation of the origin of large, quasi-stationary meanders in the jet stream.

2.1 Blockings

Blockings or blocks are persistent weather patterns in the middle to high latitudes that result from large, quasi-stationary meanders in the jet stream (Woollings et al. 2018). They literally block transient eddies and disrupt the usual zonal flow. In Fig. 2.1, a range of blocking patterns is shown, demonstrating their diversity.

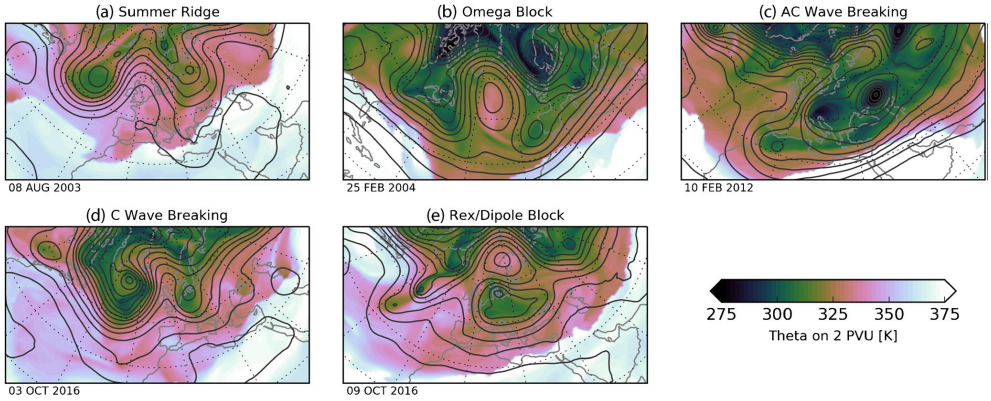

Figure 2.1: Different types of blockings over North Atlantic. Color shading shows potential temperature θ on dynamical tropopause (PV = 2PVU), 60 m spaced contour lines show 500 hPa geopotential height. Data is from ERA-Interim. Source: (Woollings et al. 2018).

One of the most typical kind of blockings is shown in Fig. 2.1a, a stationary ridge in a large scale Rossby wave, where hot air from the subtropics is advected to the mid-latitudes, causing anomalous temperature. Due to low potential vorticity of the subtropical air, it is anomalously anticyclonic in the mid-latitudes, disrupting the usual zonal flow and/or storm tracks. The ex-

ample in this figure is a snapshot of August 8th, 2003, which lies within the time frame of the European heat wave. It can be nicely seen how the high pressure system lies over the whole of Europe. This is the kind of blocking that is hypothesized to be formed by QRA.
Omega blocks are similar, however the advected air mass and high pressure is enclosed in colder temperatures and lower pressure, therefore showing closed contours of geopotential height (Fig. 2.1b). Other patterns are caused by Rossby wave breaking (Masato et al. 2012, Gabriel & Peters 2008), where the extended ridge is folded over in a cyclonic (Fig. 2.1c) or anticyclonic (Fig. 2.1d) way. For strong folding, this can lead to a dipole block as shown in Fig. 2.1e (Rex 1950).
The stages of a blocking life cycle (onset, maintenance and decay) can currently be not explained by one coherent dynamical theory (Woollings et al. 2018).
The onset usually happens on a timescale of about one to three days and involves atmospheric waves of different spatial scales interacting with each other and the background flow (Woollings et al. 2018). Nakamura et al. (1997) found that the relative importance of high and low frequency waves is dependent on the location of the block. Over Europe, quasi-stationary planetary scale Rossby waves are of primary importance for blocking onset, whereas over the North Pacific, synoptic scale eddies make the strongest contribution. Observations also suggest that some waves that are excited in the tropics propagate into the mid-latitudes and interact there with the background flow (Renwick & Revell 1999).
One major feature of blockings is the maintenance of the position of the anomaly, despite possible strong westerly flows up- and downward of the block. In the simplest case of Fig. 2.1a, this is achieved by a balance between zonal advection in the background flow and westward propagation of the Rossby wave (Woollings et al. 2018). However, for more complex blocking patterns, the dominant sustaining force are positive feedbacks of synoptic-scale eddies on the block (Shutts 1983, Mullen 1987, Austin 1980, Yamazaki & Itoh 2013). Upstream of the blocking, transient eddies are meridionally stretched and encourage wave breaking, which further intensifies the block. Block decay is usually associated with processes disrupting the maintenance mechanisms.

Intensification

Blockings are a well known cause of anomalously hot or cold weather, depending on the type and time of occurrence. Often the weather extremes caused by blockings, induce an array of feedback mechanisms that further intensifies the extreme. For example, the advection of hot dry air from the subtropics not only leads to higher temperatures, but also less humidity and therefore less rain. This can start a negative soil-moisture precipitation (SM-P) feedback loop, potentially adding droughts to the dangers of heat waves. On the other hand, warmer air can hold more water vapour. Therefore, persistent warm weather patterns can also lead to flooding. Whether the SM-P feedback loop is positive or negative, depends on the soil moisture content, as well as air temperature and humidity (Yang et al. 2018).
Clouds interact strongly with radiation depending on their altitude and with that temperature, density and albedo. Low level clouds tend to have higher albedo and higher emission temperature than high level clouds, leading to a decrease of net downward radiation at the earth's surface (short-wave cloud-radiative effect, SW CRE). High level clouds on the other hand increase the

net down flux of radiation (long-wave cloud-radiative effect, LW CRE) (Goosse et al. 2009). Whether SW CRE or LW CRE dominates depends on the season, location and properties of the clouds (Ceppi & Hartmann 2015).
In addition to soil moisture and humidity, also persistent anomalies in the dynamics of the atmosphere can affect the distribution of clouds, and therefore the energy balance of the atmosphere. For example, Black et al. (2004) found specific cloud patterns and related outgoing long-wave radiation (OLR) anomalies in the North Atlantic sector for the 2003 European heat wave, being caused by an intense Azores high, a northward shift in the inner-tropical convergence zone (ITCZ) and a southward shift of the summer storm track, that were responsible for starting a negative SM-P feedback. According to Black et al. (2004), the SM-P feedback played an important role in drying out the European land surface. The persistence of the anomalous high over Europe in June led to radiative anomalies through less cloud cover, that were balanced by a heating of the land surface and therefore increased latent and sensible heat fluxes, effectively drying out the surface. In July, when radiative anomalies reduced, a decrease of latent heat fluxes, and an increase of sensible heat fluxes due to the heating of the surface, are indicative of very low soil moisture content of the European land surface. Reduced cloud cover persisted well into August, allowing the atmosphere as well as the surface to heat up, leading to highest temperatures from 6 to 12 of August.

2.2 Quasi-resonant amplification

QRA is hypothesized to cause a blocking of the type shown in Fig. 2.1a. Two different types of atmospheric waves are the underlying driver of QRA: free and forced Rossby waves.
Free waves of synoptic scale are characterised by eastward propagation with a phase speed in the order of (6 to 12) cm/s, and by large wave numbers (k) 6 or higher (Schneider et al. 2015).
Forced waves are caused by orographic and diabatic forcings. Typically, they change on larger timescales than free Rossby waves, due to the slow changes of the underlying forcing patterns. Usual timescales are up to several weeks. Therefore, these kind of waves are called quasi-stationary. Their wave numbers (m) are usually smaller than 6. The wave number 6 to 10 component of forced waves is typically small and its wave energy can efficiently be dispersed towards the poles and equator (Kornhuber et al. 2016).
Another important part of the QRA theory are turning points (TPs). They are latitudinal positions where the square of the meridional wave number of a free Rossby wave (usually l^2, for calculation see Section 4.2) changes sign. If there exist two TPs and

- $l^2 > 0$ in between the TPs
- Zonal mean zonal wind $U > 0$ in between and in vicinity of TPs
- The TPs lie between 30°N and 70°N
- The TPs have a minimum distance $w_k \approx 2°$
- The highest value of l^2 between the TPs lies between l^2_{min} and l^2_{max}

the two TPs define a waveguide, where wave energy is trapped and cannot be dispersed above or below the latitudes of the TPs (Kornhuber et al. 2016).
If a free travelling Rossby wave gets trapped inside two TPs, its energy cannot be dispersed and therefore it might resonate with the background flow, which is the process of QRA. The necessities for QRA to occur are: *i*) a waveguide is present for a free Rossby wave with similar length scale than the forced Rossby wave, i.e. $m \approx k$ and *ii*) the thermally and orographically forced wave is of sufficient amplitude. If these criteria are fulfilled, QRA can lead to a high amplitude quasi-stationary wave, however does not necessarily have to. The detection scheme of Kornhuber et al. (2016) found the conditions to be fulfilled for 308 events, only 178 events however featured waves of sufficiently large amplitude to pass as an QRA event.
As an additional indication for a QRA event, often times the zonal mean jet profile is used. This usually features a double-spiked jet, as the one in Fig. 1.2 (Kornhuber et al. 2016). This does not necessarily mean that the mid-latitude jet is split into two meridionally distinct components, but that the jet consists of large meanders.

Typically it is assumed, that the scale of the wave (Δ_w) is much smaller than that of the background flow (Δ_b), i.e.

$$\frac{\Delta_w}{\Delta_b} \ll 1 \tag{2.1}$$

in order for Wentzel-Kramers-Brioullin (WKB) theory (Hoskins & Karoly 1981) to be valid. The equation for the meridional wavenumber is derived assuming the validity of this theory (see Section 4.2). Wirth (2020) argues that this assumption is badly violated in research done by Kornhuber et al. (2016). Further, Wirth (2020) investigates the waveguidability of idealized mid-latitude jets. The results strongly contradict the WKB theory, in the sense that waveguidability is found to smoothly increase with jet width and strength, and not like predicted by the WKB theory is either completely non-existent or perfect in the case of two turning points. Specifically: "We conclude that a literal application of ray tracing theory can be misleading; in particular, the existence of two turning latitudes is by no means a binary event at which the waveguidability suddenly changes in a fundamental way." (Wirth (2020), Section 6).
The mathematical formalism of the QRA theory, along with all the relevant equations that are used in the subsequent analyses of this thesis are derived in Section 4.2.

3 Influence of Climate Change on Heat Waves

There is strong evidence for an increase in frequency, as well as in intensity of certain types of extreme events such as heat waves in a warming climate (Coumou & Rahmstorf 2012, Rahmstorf & Coumou 2011). The cause for this increase can be broken down into two sources:

- Influence from purely thermodynamical considerations
- Influence on circulation patterns and therefore on mechanisms that produce heat waves

3.1 Thermodynamical considerations

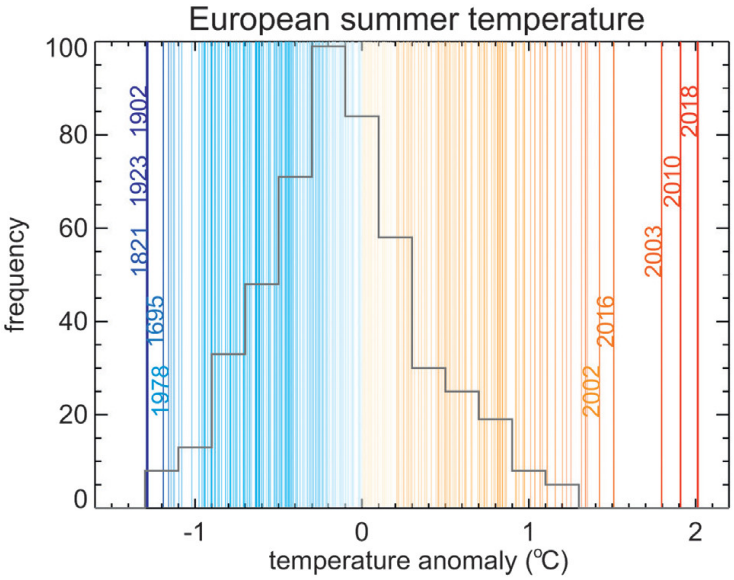

Figure 3.1: European summer temperature anomalies (°C with respect to 1981-2010 mean) over 25°W–40°E, 35°–70°N for 1500–2018 (lines) and its 1500–2000 frequency distribution (bars). Source: Barriopedro et al. (2020).

The probability distribution of summer temperatures has been shifted toward warmer values, and has been widened, due to climate change (Schär et al. 2004). This results in a higher probability of high temperatures, higher mean temperatures and an increase in maximum temperatures. Fig. 3.1 shows the anomaly of JJA mean temperatures with respect to 1981 to 2010

climatological mean, indicating a significant trend that is a result of the mentioned shift in the probability distribution. The summers of 2003, 2010 and 2018 can be seen on the far right, with anomalies of almost +2°C over the whole of Europe during the entire summer, demonstrating the severity of these events. This indicates the need of a dynamical cause for the severity of these events, since with the thermodynamical explanations alone, a frequency this high of heat waves of this magnitude is very unlikely (Luterbacher et al. 2004).

3.2 Influence on mid-latitude circulation

While the thermodynamical aspect of a warming climate is generally accepted and understood, the influence of climate change on the dynamics of relevant heat wave drivers is far more controversial, owing to the complexity of the system. The influence on dynamics can be directly on mid-latitude circulation, or indirectly via a link between Arctic weather and mid-latitude dynamics.

3.2.1 Direct influence

The direct influence of climate change on mid-latitude atmospheric dynamics is difficult to determine. However, this should give a short overview of the projected changes in terms of blocking frequency and region of occurrence, changes of the jet stream and planetary waves.

Blocking

Coupled Model Intercomparison Project Phase 5 (CMIP 5) models indicate an eastward shift of winter blocking activity that manifests as a reduction on the western flanks of the Euro-Atlantic and Pacific sector but increase on eastern sides (Woollings et al. 2018). For the Euro-Atlantic sector, the eastward shift can be directly related to a strengthening of the Atlantic jet (de Vries et al. 2013). For the Pacific however no such cause can be found, indicating that there are more complex processes responsible for these changes. Similarly, in summer poleward shifts of blocking spots are found, meaning a reduction of blocking frequency in middle latitudes and an increase in high latitudes (Woollings et al. 2018). However, these projected changes strongly depend on the index used for block identification. Models show an overall underestimation of blockings, and additionally a decline of occurrence throughout the 21st century, with strong regional and seasonal variations (Woollings et al. 2018).

Jet

In the Northern Hemisphere, CMIP5 simulations show a poleward shift of the Atlantic and Pacific eddy driven jets by 1° for Representative Concentration Pathway 8.5 (RCP 8.5) (Barnes & Polvani 2013). In the southern Hemisphere the jet is projected to migrate by even 2°. While the speed is projected to remain constant for both Northern Hemisphere jets, the variability of the jets is a strong function of jet position. While migrating poleward, the North Atlantic jet

becomes less meandering but exhibits more variations in speed, whereas the North Pacific jet is expected to meander more and have less variations in speed (Barnes & Polvani 2013). Since QRA events are often associated with a double-spiked jet such as in Fig. 1.2, these findings might have important consequences for the occurrence of QRA events in the context of climate change, depending on which change in jet variability dominates.

Storm track

Storm tracks are regions in which extratropical cyclones usually travel and are of great importance for transporting heat, momentum and moisture and therefore very influential for weather on earth, especially in the mid-latitudes (Mbengue & Schneider 2013, Shaw et al. 2016). The position of storm tracks varies seasonally, and is driven as well by sea surface temperature (SST) variations. Cyclones typically form where large temperature gradients are given, making the position of storm tracks dependent on temperature gradients as well (Shaw et al. 2016). Yin (2005) found a poleward shift of storm tracks in response to anthropogenic greenhouse-gas forcing. Additionally, recent observational studies support modelling results (Mbengue & Schneider 2013). The mechanistic understanding of this shift however remains unclear. Efforts have been made attributing the storm track shift to large scale dry-dynamics (Mbengue & Schneider 2013), as well as to associate it with mean available potential energy (MAPE) (Mbengue & Schneider (2016)). Woollings et al. (2012) show that the difference of storm track projections for the North Atlantic amongst models is due to uncertainties in ocean circulation changes.

3.2.2 AA influence

The lower Arctic atmosphere has warmed at a rate at least twice as fast than that of the the global average since 2000 (Screen & Simmonds 2010, Cohen et al. 2019, Coumou et al. 2018). This well known effect is called Arctic amplification (AA) and is mainly driven by diminishing sea ice and the resulting feedback (Screen & Simmonds 2010). In recent years, it has often been proposed that (AA) has an influence on mid-latitude circulation through changing sea ice and snow cover (Coumou et al. 2018, Cohen et al. 2014). There are three leading hypotheses on how these changes in the Arctic could affect mid-latitude circulation:

- Shift in storm tracks
- Weakening of the jet stream
- Amplification of quasi-stationary planetary waves

Fig. 3.2 shows a huge variety of factors influencing these components of mid-latitude circulation, only one of which is AA, which itself is influenced by other factors. This demonstrates the complexity of the hypothesized linkages. Cohen et al. (2014) published an detailed overview on the link between AA and mid-latitude circulation, which describes the mechanisms behind the possible changes:

Storm tracks

The main source of internal variability for the position of storm tracks is the North Atlantic Oscillation/Arctic Oscillation (NAO/AO). In positive phases of NAO/AO, storm tracks shift poleward, in negative phases equatorward. Changes in Arctic sea ice cover, as well as Eurasian snow cover might affect the amplitude and phase of NAO/AO and consequently shift the storm tracks. The phase of the NAO/AO also influences the surface temperature distribution in the Northern Hemisphere: in its positive phase, winters are mild across Eurasia and severe in the Arctic, whereas in its negative phase it's the opposite. This is an important contributing factor when it comes to possible dynamical changes in the jet stream. Modelling studies show more tendency towards a negative response of the NAO/AO to diminishing sea ice. However, this response is small compared to natural variability.

Jet

A faster warming of higher latitudes compared to lower or mid-latitudes reduces the meridional surface temperature gradient. This gradient is a fundamental driver of the zonal jet stream. Through the thermal wind relationship, a smaller meridional surface temperature gradient could produce a weaker jet with larger meanders. However, it is important to note that while the surface temperature gradient weakens, at higher altitudes the opposite is the case: the tropics warm faster than high latitudes and increase the meridional gradient, therefore potentially strengthening the jet. This is the so called tug-of-war (Barnes & Screen 2015), that needs a lot more research to be understood and applied to statements about changes in the jet.
Not only does the meridional temperature gradient influence the jet, but also larger meanders in the jet influence the meridional temperature gradient. Currently it is not understood whether this is a positive (intensifying) or negative (stabilizing) feedback.
Additionally, internal seasonal variability through the NAO/AO which is not understood in the context of climate change and AA is another contributing factor that influences this temperature gradient, making the overall response of this linkage to climate change seasonally dependent.
The jet is not only thermally driven, but also consists of an eddy driven part that in turn influences the temperature gradient. Stratospheric winds, such as the polar jet influence the propagation of planetary waves, that in turn impact the mid-latitude jet. These are two way feedbacks that are non-linear and therefore of vast complexity.

Planetary waves

Extensive autumn snow cover over Eurasia has been linked to larger high-latitude planetary waves, with stronger vertical propagation of wave energy, eventually causing a warmer and weaker polar jet after a time lag of a few weeks, in turn influencing high-latitude dynamics and wave structures. Another important issue are Barents and Kara sea ice anomalies, enabling cold-air advection over northern Europe by affecting the AO, which in turn can have an influence on the wave structure.

There is a wide range of outcomes from studies analysing these linkages (Cohen et al. 2019). While there is consensus that AA *can* affect mid-latitude circulation and therefore possibly heat

wave mechanisms, the definitive outcome of the change is hard to predict, owing to the complexity of the system (Barnes & Screen 2015). Observational studies are suggesting the contribution of AA to continental winter cooling, while models disagree (Cohen et al. 2019). The fact that other hypothesized linkages are not observed, may be because the effects are too weak to be observed on top of natural variability, or due to incomplete mechanistic understanding of the underlying, non-linear processes.
Another important aspect is the issue of causality. It is understood that mid-latitude weather patterns influence the Arctic weather (Graversen 2006, Screen et al. 2012). Therefore, the question whether it is mid-latitude forcings driving AA, rather than the other way around, should be raised (Screen et al. 2012, Barnes & Screen 2015).

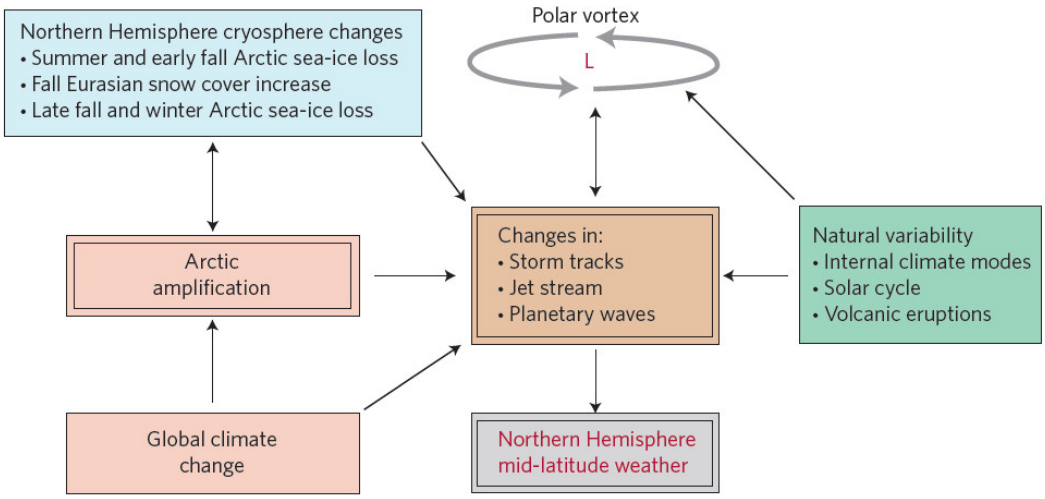

Figure 3.2: Schmeatic of ways to influence mid-latitude circulation. Source: Cohen et al. (2014).

4 Data and Methods

For Sections 5.1, 5.2, 5.11 and 6 daily data from the European Centre for Medium-Range Weather Forecasts (ECMWF) ERA-Interim reanalysis in 2.5° zonal and 2.5° meridional resolution was used (Dee et al. 2011). For Section 5.10 GISTEMP (Lenssen et al. (2019), GISTEMP(2020)) and HadCRUT4 (Morice et al. 2012) data was used. Monthly or daily data, depending on availability of the three randomly selected CMIP5 models (HadGem2-AO (Martin et al. 2011), CNRM-CM5 (Voldoire et al. 2013), IPSL-CM5A-LR (Dufresne et al. 2013)) was used in Section 5.3.3.
All analyses were done using Python 3. Trends were calculated by performing linear regressions, and the correlation coefficients that were calculated always refer to the Pearson correlation (Wilks 2006).

4.1 QRA Detection Algorithm

Kornhuber et al. (2016) developed a detection scheme to analyse the occurrence and properties such as duration, wave numbers and amplitude of QRA events in the past. The detection conditions are

1. For a free synoptic scale wave with zonal wave number k, a waveguide fulfilling the requirements presented in Section 4.2 is present

2. The effective forcing amplitude A_{eff} of the forced Rossby wave with wave number $m \approx k$ has to exceed a certain threshold q_k.

Using the same detection algorithm and data, no QRA events were found in the research for this thesis. The problem with the implementation as presented in this thesis was, that no waveguides and therefore no QRA events could be detected for the summer months (June, July and August, JJA) from 1979 to 2015. As an illustrative example see Fig. 4.1, that shows the latitudinal distribution of the square of the meridional wavenumber for JJA during the summer heat wave of Europe in 2003. A waveguide would have been drawn if it was found by the detection algorithm, similar to Fig. 1c by Kornhuber et al. (2016). Comparing this result to the one produced by Kornhuber et al. (2016), two noticeable features are different. These are the two areas of red (i.e. positive wavenumber l^2) and blue (i.e. negative wavenumber l^2) in the end of June (red) and July (blue). The blue area in late July / beginning of August is where the waveguide was found by Kornhuber et al. (2016). This is a surprising result, since the same data was used, as can be seen when comparing Fig. 4.2 in this thesis and Fig. 1a in Kornhuber et al. (2016).

A lot of thought was given to the source of the potential error. Individual terms of the formula for the meridional wave number (i.e. Eq. 4.2) were analysed for the potential source. However, the results of calculation seemed to be a logical outcome of the data that was fed into the

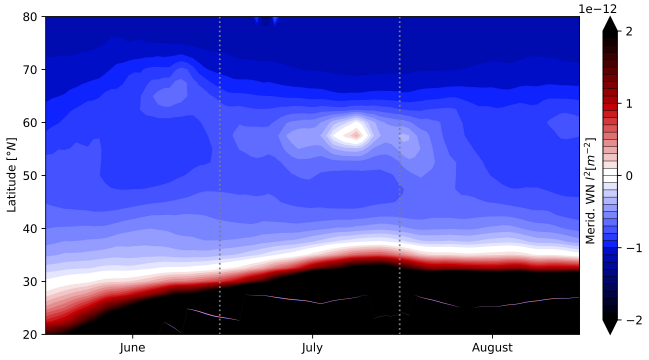

Figure 4.1: Squared meriodional wavenumber l of June, July and August in 2003.

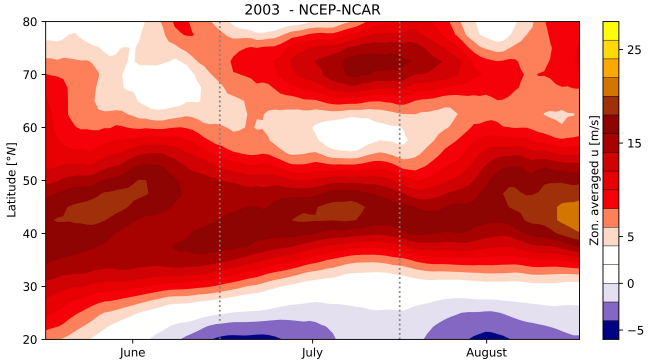

Figure 4.2: Zonally averaged zonal wind field for June, July and August in 2003. This data was used for the calculation of the square of the meridional wavenumber l^2.

equation. Additionally, different datasets have been used (i.e. National Center for Environmental Prediction's and the National Center for Atmospheric Research's (NCEP-NCAR) (Kalnay et al. 1996) and ERA-Interim reanalysis (Dee et al. 2011)) with a variety of resolutions, which all failed to produce the features that were found by Kornhuber et al. (2016), who used NCEP-NCAR data with a meridional and longitudinal resolution of 2.5°. Taking into account possible numerical issues due to the small magnitude of the wave number (i.e. $l^2 \approx 10^{-13}$) did not make a difference. Finally different methods for calculating the necessary gradients were implemented but the results also did not show any waveguides.
The dates and durations of detected wave number 7 QRA events with a duration greater than 10 days used for the analysis in Section 5 were then provided by Kai Kornhuber and are listed in Tab. 4.1.

Table 4.1: QRA events with zonal wave number $k = 7$ and duration greater than 10 days. Used for analyses in Section 5. Provided by Kai Kornhuber.

7. June - 16. June 1980	30. June - 16. July 2001
14. July - 29. July 1983	15. July - 6. August 2003
11. August - 31. August 1984	4. June - 29. June 2006
20. July - 4. August 1984	11. July - 24. July 2006
11. June - 14. July 1986	22. July - 10. August 2008
10. August - 29. August 1989	9. July - 25. July 2009
14. August - 25. August 1992	24. June - 4. July 2009
21. July - 16. August 1994	8. August - 19. August 2011
7. June - 1. July 1996	24. July - 11. August 2012
2. June - 12. June 1997	16. June - 29. June 2013
1. June - 11. June 2000	15. July - 27. July 2014
1. June - 19. June 2001	25. July - 18. August 2015

4.2 Mathematical Formalism of QRA

I will derive the geostrophic relationship and the vorticity equation from the momentum equations. Then, by assuming barotropy and a confined flow, I will derive wave equations for which free travelling and forced stationary Rossby waves are solutions. Finally, waveguides as well as other important assumptions and their role in the QRA mechanism will be derived from the wave equations projected onto a spherical atmosphere.

Momentum equations and geostrophic relationship

The Navier-Stokes or momentum equations describe the movement of a parcel of air which is determined by the forces acting on the parcel. These are the Coriolis, gravitational, friction and the pressure gradient force. With the material derivative $\frac{D}{Dt} = \frac{\partial}{\partial t} + \vec{u} \cdot \vec{\nabla}$, they can be written as (Lynch & Cassano 2006):

$$\frac{Du}{Dt} = -\frac{1}{\rho}\frac{\partial p}{\partial x} + \nu(\frac{\partial^2 u}{\partial x^2} + \frac{\partial^2 u}{\partial y^2} + \frac{\partial^2 u}{\partial z^2}) + (2\Omega v \sin\phi - 2\Omega w \cos\phi) \tag{4.1}$$

$$\frac{Dv}{Dt} = -\frac{1}{\rho}\frac{\partial p}{\partial y} + \nu(\frac{\partial^2 v}{\partial x^2} + \frac{\partial^2 v}{\partial y^2} + \frac{\partial^2 v}{\partial z^2}) + 2\Omega u \sin\phi \tag{4.2}$$

$$\frac{Dw}{Dt} = -g - \frac{1}{\rho}\frac{\partial p}{\partial z} + \nu(\frac{\partial^2 w}{\partial x^2} + \frac{\partial^2 w}{\partial y^2} + \frac{\partial^2 w}{\partial z^2}) + 2\Omega u \cos\phi \tag{4.3}$$

Now, we split the pressure field into two parts:

$$p(z) = p_0(z) + p_d \tag{4.4}$$

Here, $p_0(z)$ follows the hydrostatic balance

$$\frac{dp_0}{dz} = -\rho_0 g \tag{4.5}$$

and p_d describes deviations from this balance. The horizontal momentum equations now have a p_d, whereas the vertical momentum equation now can be expressed in terms of the hydrostatic balance:

$$\frac{Du}{Dt} = -\frac{1}{\rho}\frac{\partial p_d}{\partial x} + \nu(\frac{\partial^2 u}{\partial x^2} + \frac{\partial^2 u}{\partial y^2} + \frac{\partial^2 u}{\partial z^2}) + (2\Omega v \sin\phi - 2\Omega w \cos\phi) \tag{4.6}$$

$$\frac{Dv}{Dt} = -\frac{1}{\rho}\frac{\partial p_d}{\partial y} + \nu(\frac{\partial^2 v}{\partial x^2} + \frac{\partial^2 v}{\partial y^2} + \frac{\partial^2 v}{\partial z^2}) + 2\Omega u \sin\phi \tag{4.7}$$

$$\frac{Dw}{Dt} = -\frac{(\rho - \rho_0)}{\rho} g - \frac{1}{\rho}\frac{\partial p_d}{\partial z} + \nu(\frac{\partial^2 w}{\partial x^2} + \frac{\partial^2 w}{\partial y^2} + \frac{\partial^2 w}{\partial z^2}) + 2\Omega u \cos\phi \tag{4.8}$$

We introduce a non-dimensional parameter which we will call the *Rossby number*(Ro) and define it as the ratio of the inertial term to the Coriolis term of the momentum equation (Lynch & Cassano 2006):

$$Ro = \frac{\partial u/\partial t}{(2\Omega v \sin\phi - 2\Omega w \cos\phi)} \tag{4.9}$$

For $Ro \to 0$ the resulting flow is termed geostrophic. This is usually the case for a mid-latitude cyclone. Doing a scale analysis justifies neglecting the friction force and vertical advection terms $w\frac{\partial u}{\partial z}$ and $w\frac{\partial v}{\partial z}$ in the horizontal momentum equations, leaving us with

$$\frac{\partial u}{\partial t} + u\frac{\partial u}{\partial x} + v\frac{\partial u}{y} = -\frac{1}{\rho}\frac{\partial p_d}{\partial x} + 2\Omega v \sin\phi \tag{4.10}$$

$$\frac{\partial v}{\partial t} + u\frac{\partial v}{\partial x} + v\frac{\partial v}{y} = -\frac{1}{\rho}\frac{\partial p_d}{\partial y} - 2\Omega u \sin\phi \tag{4.11}$$

Also inserting characteristic scales for horizontal wind derivatives $\frac{\partial u,v}{\partial x}$ and $\frac{\partial u,v}{\partial y}$ indicate a small error contribution by neglecting these terms. Since we assume a static basic wind state (i.e. $\frac{\partial u}{\partial t} = 0$, the resulting equation is therefore only diagnostic and cannot be used for prediction), we obtain finally for the synoptic scale horizontal momentum equations

$$\frac{1}{\rho}\frac{\partial p_d}{\partial x} = 2\Omega v \sin\phi \tag{4.12}$$

$$\frac{1}{\rho}\frac{\partial p_d}{\partial y} = -2\Omega u \sin\phi \tag{4.13}$$

With the Coriolis parameter $f = 2\Omega \sin\Phi$ and solving for the wind components yields the geostrophic wind relationship:

$$u_g = -\frac{1}{\rho f}\frac{\partial p_d}{\partial y} \tag{4.14}$$

$$v_g = \frac{1}{\rho f}\frac{\partial p_d}{\partial x} \tag{4.15}$$

Vorticity Equation

We introduce a new quantity called vorticity ω, which is the curl of the wind field (Lynch & Cassano 2006), i.e.

$$\vec{\omega} = \vec{\nabla} \times \vec{u} = \begin{pmatrix} \frac{\partial w}{\partial y} - \frac{\partial v}{\partial z} \\ \frac{\partial u}{\partial z} - \frac{\partial w}{\partial x} \\ \frac{\partial v}{\partial x} - \frac{\partial u}{\partial y} \end{pmatrix} \tag{4.16}$$

The z-component of the vorticity $\omega_z = \xi$ is usually the dominant one since vertical velocities and vertical advection are $\approx 10^{-2}$ orders smaller than horizontal velocities and horizontal advection. We can find an equation for ξ by taking the derivative of

$$\frac{Du}{Dt} = -\frac{1}{\rho}\frac{\partial p_d}{\partial x} + fv$$

with respect to y:

$$\frac{D_h}{Dt}\Big(\frac{\partial u}{\partial y}\Big) = -\frac{1}{\rho}\frac{\partial^2 p_d}{\partial x \partial y} + f\frac{\partial v}{\partial y} + v\frac{\partial f}{\partial y} \tag{4.17}$$

Now, taking the derivative of

$$\frac{Dv}{Dt} = -\frac{1}{\rho}\frac{\partial p_d}{\partial y} - fu$$

with respect to x yields

$$\frac{D_h}{Dt}\Big(\frac{\partial v}{\partial x}\Big) = -\frac{1}{\rho}\frac{\partial^2 p_d}{\partial x \partial y} - f\frac{\partial u}{\partial x} - u\frac{\partial f}{\partial x} \tag{4.18}$$

We subtract (3.17) from (3.18) and get:

$$\frac{D_h}{Dt}\Big(\frac{\partial v}{\partial x} - \frac{\partial u}{\partial y}\Big) = -f\Big(\frac{\partial u}{\partial x} + \frac{\partial v}{\partial y}\Big) - u\frac{\partial f}{\partial x} - v\frac{\partial f}{\partial y}$$

Here, the terms with the second derivative of the dynamical pressure p_d cancel, and we assume that the density does not vary significantly horizontally (i.e. $\frac{\partial}{\partial x,y}\frac{1}{\rho} = 0$). Identifying the z-component of the vorticity $\omega_z = \xi$ in this equation leads to:

$$\frac{D_h \xi}{Dt} + u\frac{\partial f}{\partial x} + v\frac{\partial f}{\partial y} = -f\Big(\frac{\partial u}{\partial x} + \frac{\partial v}{\partial y}\Big)$$

Furthermore, $\frac{\partial f}{\partial t} = 0$ and therefore

$$\frac{D_h}{Dt}(\xi + f) = -f\Big(\frac{\partial u}{\partial x} + \frac{\partial v}{\partial y}\Big)$$

From the continuity equation of a barotropic fluid (Lynch & Cassano 2006) it follows that:

$$\frac{\partial u}{\partial x} + \frac{\partial v}{\partial y} = -\frac{\partial w}{\partial z} \tag{4.19}$$

Therefore we get for the barotropic vorticity equation:

$$\frac{D_h}{Dt}(\xi + f) = f\frac{\partial w}{\partial z} \tag{4.20}$$

Flow

We assume now that the flow of the fluid is confined between one lower boundary $h_b(x,y,t)$ that is variable in space (i.e. mountain chains), and an upper boundary at the tropopause at constant height H_t. Integrating Eq. 4.20 vertically, yields

$$h\frac{D_h(\xi+f)}{Dt} = f\Big(w(H_t) - w(h_b(x,y,t))\Big) \tag{4.21}$$

With $h = H_t - h_b(x,y)$. The velocities van be expressed as the material derivatives of the bottom and top layer heights. The top layer is at constant height, meaning $\frac{DH_t}{Dt} = 0$ and we get:

$$\frac{D_h(\xi+f)}{Dt} = -\frac{f}{h}\frac{D}{Dt}h_b(x,y,t) \tag{4.22}$$

Using Eq. 4.14 and Eq. 4.15 to write ξ in the geostrophic approximation we get

$$\xi = \frac{\partial v}{\partial x} - \frac{\partial u}{\partial y} = \frac{1}{\rho f}\frac{\partial^2 p_d}{\partial x^2} + \frac{1}{\rho f}\frac{\partial^2 p_d}{\partial y^2} = \frac{1}{\rho f}\vec{\nabla}^2 p_d = \frac{1}{f}\vec{\nabla}^2\Phi = \vec{\nabla}^2\psi \tag{4.23}$$

with the geopotential height $\Phi = gz = \frac{p}{\rho}$ and the definition of the streamfunction ψ (Pedlosky & Robertson 1988)

$$\psi = \frac{\Phi}{f} \tag{4.24}$$

The operator $\frac{D_h}{Dt}$ can be expressed as

$$\frac{D_h}{Dt} = \frac{\partial}{\partial t} + \vec{u}\cdot\vec{\nabla} = \frac{\partial}{\partial t} - \frac{\partial\psi}{\partial y}\frac{\partial}{\partial x} + \frac{\partial\psi}{\partial x}\frac{\partial}{\partial y} \tag{4.25}$$

since $u = -\frac{\partial\psi}{\partial y}$ and $v = \frac{\partial\psi}{\partial x}$ (Pedlosky & Robertson 1988). Thus the barotropic vorticity equation (4.20) conveniently takes the form

$$\frac{D_h}{Dt}\vec{\nabla}^2\psi + \beta\frac{\partial\psi}{\partial x} = -\frac{f}{h}\frac{D}{Dt}h_b(x,y,t) \tag{4.26}$$

where we used the beta-plane approximation $f = 2|\Omega|\sin\Phi_0 \approx f_0 + \beta y$ (Lynch & Cassano 2006) with $\beta = 2|\Omega|\frac{\cos(\Phi_0)}{a}$, and a the mean radius of the earth.
Additionally, we can have a homogeneous wave equation, for which the right hand side of 4.26 is zero. This would be the case when we assume a horizontal lower boundary $h_b \neq h_b(x,y)$, i.e. $\frac{Dh_b}{Dt} = 0$. The solution for the homogeneous wave equation are free travelling Rossby waves, and for the inhomogeneous wave equation (4.26), they are forced stationary Rossby waves.
We can now linearise 4.26 by using a small perturbation in the form of

$$\psi = \bar{\psi} + \psi' = \bar{u}y + const. + \psi' \tag{4.27}$$

yielding

$$homogeneous: \Big(\frac{\partial}{\partial t} + \bar{u}\frac{\partial}{\partial x}\Big)\vec{\nabla}^2\psi' + \beta\frac{\partial\psi'}{\partial x} = 0 \tag{4.28}$$

$$inhomogeneous: \Big(\frac{\partial}{\partial t} + \bar{u}\frac{\partial}{\partial x}\Big)\vec{\nabla}^2\psi' + \beta\frac{\partial\psi'}{\partial x} = -\frac{f}{H_t}\bar{u}\frac{\partial h}{\partial x} \tag{4.29}$$

Rossby waves

For the homogeneous solution we look for 2 dimensional waves described by zonal wave number k, meridional wave number l and frequency ν:

$$\psi' = Ae^{i(kx+ly-\nu t)} \tag{4.30}$$

We calculate the dispersion relation:

$$(-\nu + k\bar{u})(-k^2 - l^2) + k\beta = 0 \tag{4.31}$$

$$\nu = \bar{u}k - \beta\frac{k}{k^2+l^2} \tag{4.32}$$

$$c_x - \bar{u} = -\frac{\beta}{k^2+l^2} \tag{4.33}$$

with $c_x = \nu/k$.
For the inhomogeneous solution we can define a surface describing the topography as

$$h(x,y) = h_0 \sin(kx+ly) \tag{4.34}$$

Stationary, two-dimensional waves with zonal wave number k and meridional wave number l then take the form

$$u = -lA\cos(kx+ly) \tag{4.35}$$

$$v = kA\cos(kx+ly) \tag{4.36}$$

Substituting this into Eq. 4.26 gives us a formula for the amplitude:

$$A = \frac{fh_0}{H}\frac{1}{\left(|\vec{k}|^2 - |\vec{k_s}|^2\right)} \tag{4.37}$$

In this formula for the amplitude, $\vec{k}$ is the wave number vector of the free travelling wave, whereas $k_s = \frac{\beta}{\bar{u}}$ is the wave number of the stationary forced wave, for which the phase speed is zero. When $|\vec{k}|^2 \approx |\vec{k_s}|^2$ this amplitude becomes very large, which is the process of quasi-resonant amplification. This can happen when a waveguide is present.

Waveguide

An important concept of the QRA-theory is that of waveguides, which can be thought of as latitudinal bands where wave energy is efficiently trapped by reflection on so called turning points. These emerge from the mathematical formalism of the QRA theory when the curvature of the earth is taken into account, which was not done in the previous derivation. In this section we will start from an wave equation in spherical coordinates, therefore arriving at a different version of Eq. 4.28, from which we can calculate a relation between meridional wavenumber l and the

zonal mean zonal wind U and latitude ϕ.

The quasi-linear barotropic vorticity equation on a sphere at the equivalent barotropic level (EBL, 300mb - 500 mb) (Hoskins & Karoly 1981) is given as:

$$\Big(\frac{\partial}{\partial t}+\frac{U}{a\cos(\phi)}\frac{\partial}{\partial\lambda}\Big)\Delta\psi+\Big(2\Omega-\frac{\Delta U}{a\cos(\phi)}\Big)\frac{\partial\psi}{\partial\lambda}=0 \tag{4.38}$$

where λ is the longitude, ϕ the latitude, t the time, a is the earth radius, Ω the earth angular velocity and U the zonal mean zonal wind. The solutions for this type of equation are free adiabatic atmospheric waves. Using a Mercator projection (Phillips, N. A. 1973) we can rewrite this equation in a more convenient expression. The Coordinates take the form

$$x=a\lambda \tag{4.39}$$

$$y=aln[(1+\sin x)/\cos x] \tag{4.40}$$

with the transformation of the differentials

$$\frac{\partial}{\partial\phi}=\frac{a}{\cos\phi}\frac{\partial}{\partial y} \tag{4.41}$$

$$\frac{\partial}{\partial\lambda}=a\frac{\partial}{\partial x} \tag{4.42}$$

With these coordinates, Eq. 4.38 takes the form

$$\Big(\frac{\partial}{\partial t}+\frac{U}{\cos\phi}\frac{\partial}{\partial x}\Big)\Big(\frac{\partial^2}{\partial x^2}+\frac{\partial^2}{\partial y^2}\Big)\psi+\Big(\frac{2\Omega}{a}\cos^2\phi-\frac{d}{dy}\frac{1}{\cos^2\phi}\frac{d}{dy}(U\cos\phi)\Big)\frac{\partial\psi}{\partial x}=0 \tag{4.43}$$

Inserting a free plane wave solution of the form

$$\psi=e^{i(Kx+ly-\omega t)} \tag{4.44}$$

into Eq. 4.43 leads to

$$\Big(i\omega-\frac{iU*K}{\cos\phi}\Big)\Big(K^2+l^2\Big)\psi+\Big(\frac{2\Omega}{a}\cos^2\phi-\frac{d}{dy}\frac{1}{\cos^2\phi}\frac{d}{dy}(U\cos\phi)\Big)iK\psi=0 \tag{4.45}$$

After rearranging and dividing by i we get

$$\omega=\frac{U}{\cos\phi}K-\frac{K}{K^2+l^2}\Big(\frac{2\Omega}{a}\cos^2\phi-\frac{d}{dy}\frac{1}{\cos^2\phi}\frac{d}{dy}(U\cos\phi)\Big) \tag{4.46}$$

We are interested in quasistationary wave solutions, meaning that we can set $\omega\approx 0$. Rearranging to l^2 and inserting the differential from Eq. 4.42 leads to the latitudinal distribution of the square of the meridional wavenumber, depending on the zonal mean zonal wind ($l^2(U,\phi)$):

$$l^2=\frac{\Omega\cos\phi}{aU}-\frac{\cos^2\phi}{a^2U}\frac{d^2U}{d\phi^2}+\frac{\sin(\phi)\cos(\phi)}{a^2U}\frac{dU}{d\phi}+\frac{1}{a^2}-K^2 \tag{4.47}$$

5 Fingerprint Analysis

The fingerprint as defined by M17 is based on the difference between the zonal and episodal means of surface temperature during certain QRA events and the JJA surface zonal mean temperature climatology. The QRA events were selected amongst the output of the detection algorithm from Kornhuber et al. (2016). The criteria are that they were wavenumber 7 events, with a duration longer than 10 days and that they happened in summer (June, July or August). The difference between the two climatologies was then interpolated to a meridional resolution of 5 degrees and centered on zero, to form the fingerprint.
Addressing the influence of climate change on QRA, M18 projected the fingerprint onto yearly JJA zonal mean temperature fields as simulated by a selection of CMIP5 models.
One very important assumption made by M18 is that the relationship between QRA surface temperature anomaly and JJA climatology stays the same throughout climate change. However, as presented in Section 3, there are a lot of climate change influences on mid-latitude circulation, and with that also on the zonal mean meridional temperature gradient that is used to define the fingerprint. These influences include indirect drivers such as AA in the lower, or tropical warming in the upper troposphere, as well as direct drivers on blocking mechanisms, jet and storm tracks. The complexity of this subject asks for a more complete picture of the atmosphere that not only takes possible changes to the surface temperature gradient into account, but also includes climate change influences higher up in the atmosphere.
In this Chapter, the concept of the QRA fingerprint as defined by M17 is reviewed and extended to various pressure levels in order to get a fuller picture of the atmosphere during a QRA event. In Section 5.1, the internal variability of the JJA climatology, as well as the QRA events is analysed for various pressure levels. This was calculated for all available ERA-Interim pressure levels, however is only presented for 300 hPa and 1000 hPa in this Section. In Section 5.2 the vertical structure of the fingerprint is analysed. Finally, in Section 5.3 the fingerprint is projected on yearly JJA climatologies to analyse temporal evolution of the coefficient for selected pressure levels (again, only 300 hPa and 1000 hPa are shown), using ERA-Interim, obervational (GISTEMP and HadCrut4) and CMIP5 data.

5.1 Internal variability

The first analysis was done by looking into the internal variability of JJA climatologies for 300 hPa and 1000 hPa pressure levels and is shown in Figs. 5.2 and 5.1, respectively. For 1000 hPa, the spread seems to be highest in the mid-latitudes, around 55°N to 65°N. Other than that, the standard deviation is quite low. For 300 hPa, the spread is larger across all latitudes, and largest in the subtropics and Arctic.

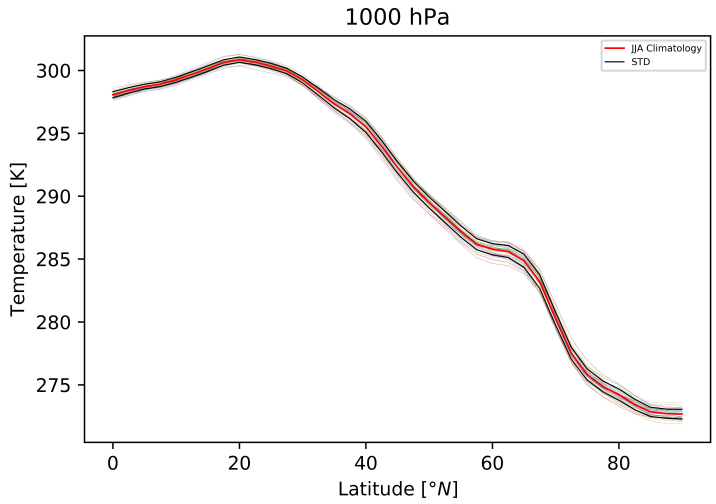

Figure 5.1: Thin colored lines are yearly JJA temperature means at 1000 hPa from 1979 to 2015, using ERA Interim data. Red line is overall temporal mean, black lines are standard deviation.

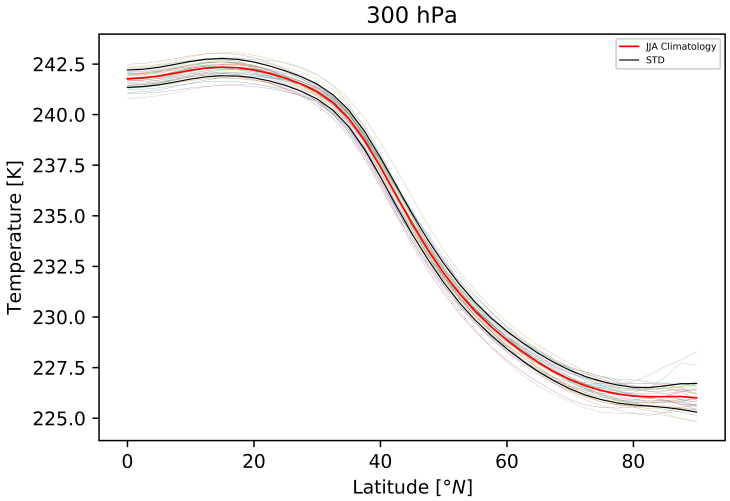

Figure 5.2: Same as Fig. 5.2 but for 300 hPa temperature data.

When looking at the zonal temperature means from QRA events from Tab. 4.1 at 300 hPa (Fig. 5.3) and 1000 hPa (Fig. 5.4) the spread, as well as the standard deviation is larger. On the surface, it is again largest at around 55°N to 65°N. For the 300 hPa data the spread is again larger across all latitudes and largest in the Arctic. Also, the difference between the dotted blue line (overall mean of QRA days) and the red line (overall mean of episodal QRA means), should be noted.

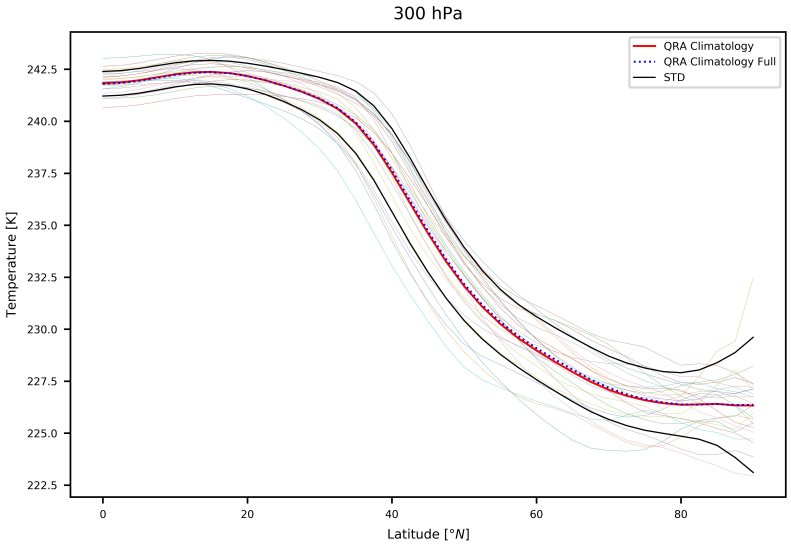

Figure 5.3: Thin colored lines are QRA episodal temperature means at 300 hPa for the events listed in Tab 4.1, using ERA Interim data. The red line shows the overall mean of the episodal means (i.e. of the thin lines), whereas the dotted blue line shows overall mean of QRA days, without taking episodal means beforehand. Black line is standard deviation of episodal means.

Figs. 5.5 and 5.6 now show a direct comparison of JJA and QRA climatologies and the respective individual seasonal/episodal means as well as the JJA standard deviation. The QRA climatology lies for all latitudes within one standard deviation of the JJA climatology, for both 300 hPa and 1000 hPa levels (this is true also for all other levels that were investigated, but not shown here). This raises the question whether the fingerprint is a strong enough signal, i.e. whether it is stronger than the internal variability of the JJA climatology. Additionally, QRA event means lie on the positive and negative side of the JJA climatology (with a large spread), as opposed to on only the positive side as could be concluded from the fingerprint. The fingerprints in this thesis for individual pressure levels are calculated as the difference between overall means of QRA days and JJA climatologies (i.e. orange line in top right panel of Fig. 5.7). The reasoning being that this is closer to the fingerprint calculated by M17. However, the fingerprint calculated here is approximately only half in amplitude. The reasons for this are unclear, since the same data was used.

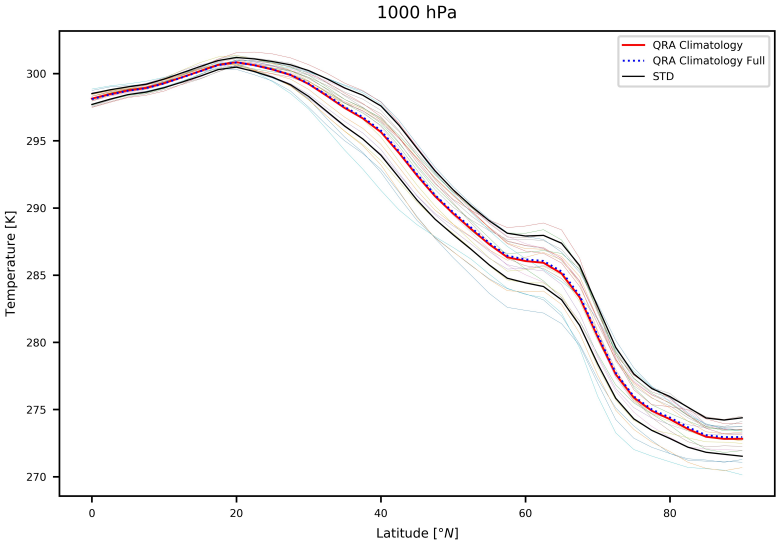

Figure 5.4: Same as Fig. 5.3 but for 1000 hPa temperature data.

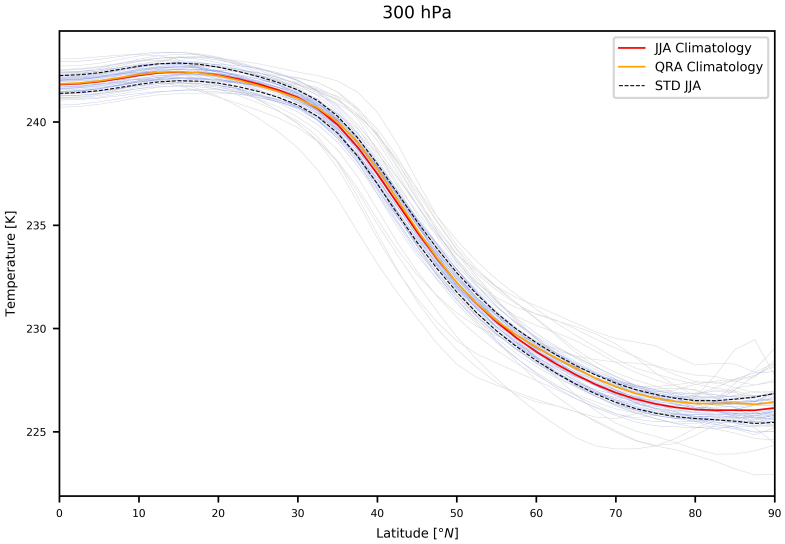

Figure 5.5: Thin gray lines are QRA episodal temperature means at 300 hPa, thin blue lines are yeary JJA temperature means at 300 hPa from 1979 to 2015. Red line shows JJA temperature climatology. Orange line shows QRA climatology, as dotted blue line in Fig. 5.3. Dotted black line is standard deviation of JJA climatology.

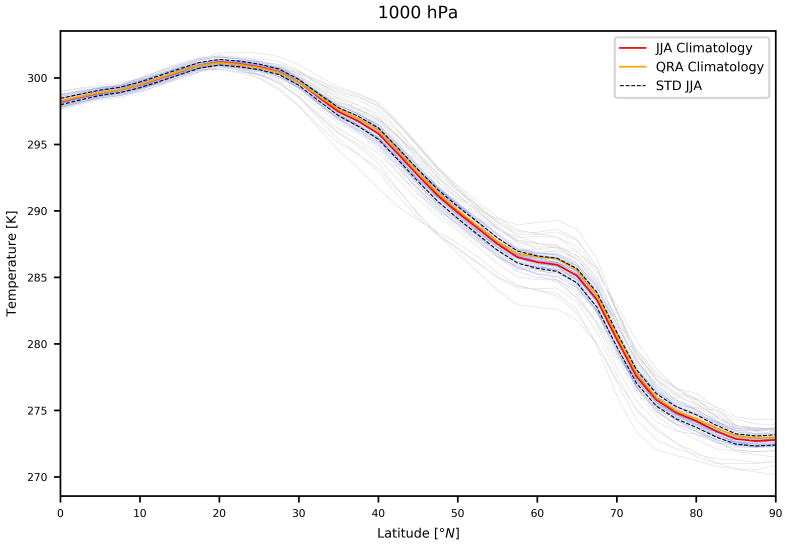

Figure 5.6: Same as Fig. 5.5 but for 1000 hPa temperature data.

The next step in the analysis was recreating Fig. 1 from M17 for surface temperature data (Fig. 5.7), as well as creating the same plot for the 300 hPa level temperature field (Fig. 5.8). Both fingerprints feature a similar structure, namely two peaks at 40°N and 65°N and minima at 25°N, 55°N and 75°N). The peak at 40°N and minimum at 75°N are less pronounced for the 300 hPa fingerprint. However, the minimum at 55°N for the 300 hPa is more than twice as large as the 1000 hPa counterpart. The maximum for the 1000 hPa fingerprint lies within the latitudinal region of the largest spread in the JJA climatology (see Fig. 5.1). Also of great interest are the temperature gradients (bottom right panels of Figs. 5.7 and 5.8), which show little similarity. Respective QRA and JJA temperature gradients are almost identical, however the 300 hPa and 1000 hPa levels show very different features. M18 used the surface temperature gradient from 55°N to 66°N (which is negative) to calculate an influence on the jet stream via the thermal wind equation. However, this equation is meant to be applied to the mean virtual temperature gradient of the 1000 hPa to 300 hPa layer, not only the surface gradient. Taking a look at the temperature gradient in Fig. 5.8 for the 300 hPa layer, it is still negative in this area, but a lot weaker. This raises the question whether there are preferred layers for the calculation of the jet stream via the thermal wind equation, or whether all the depth of the layer is needed. Section 6 will be dedicated to answer this question. It should be noted that the surface temperature gradient 55°N and 65°N is getting smaller towards the pole, the 300 hPa temperature gradient however is getting larger towards the pole.

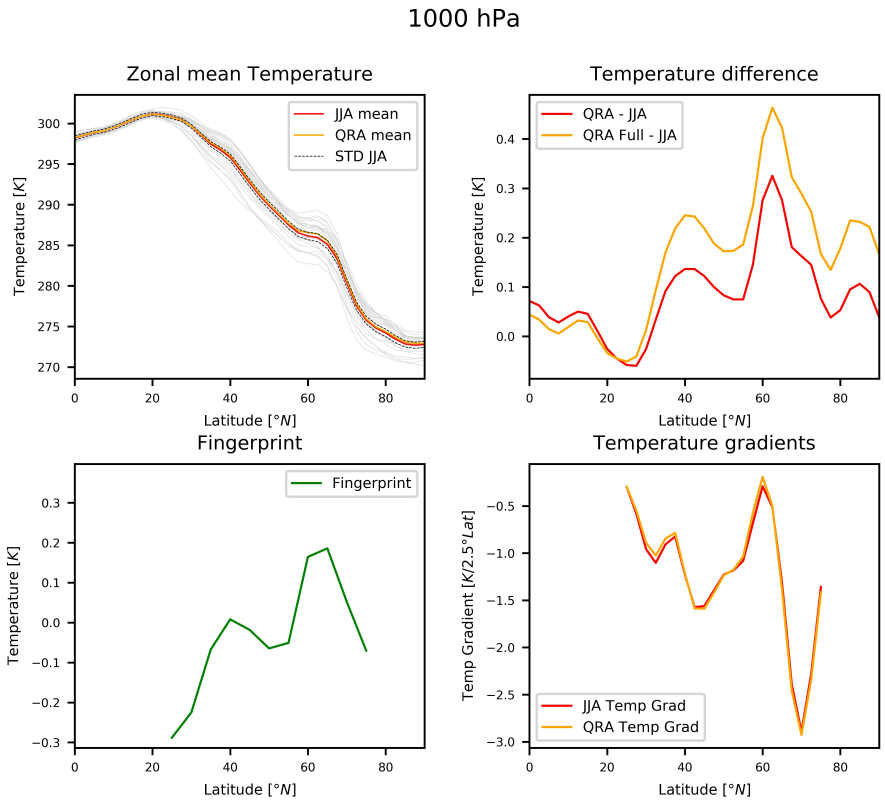

Figure 5.7: Fingerprint plot after M17. Top left panel shows Fig. 5.6. Top right panel shows differences between JJA climatology and overall mean of QRA episodal means (red) as well as JJA climatology and overall mean of QRA days (orange, also denoted as QRA Full). Bottom left panel shows fingerprint defined as the orange line from top right panel centered on zero, interpolated to a 5 degree grid and restricted to mid-latitude area 25°N to 75°N. Bottom right panel shows the calculated temperature gradients of QRA (orange) and JJA (red) climatologies.

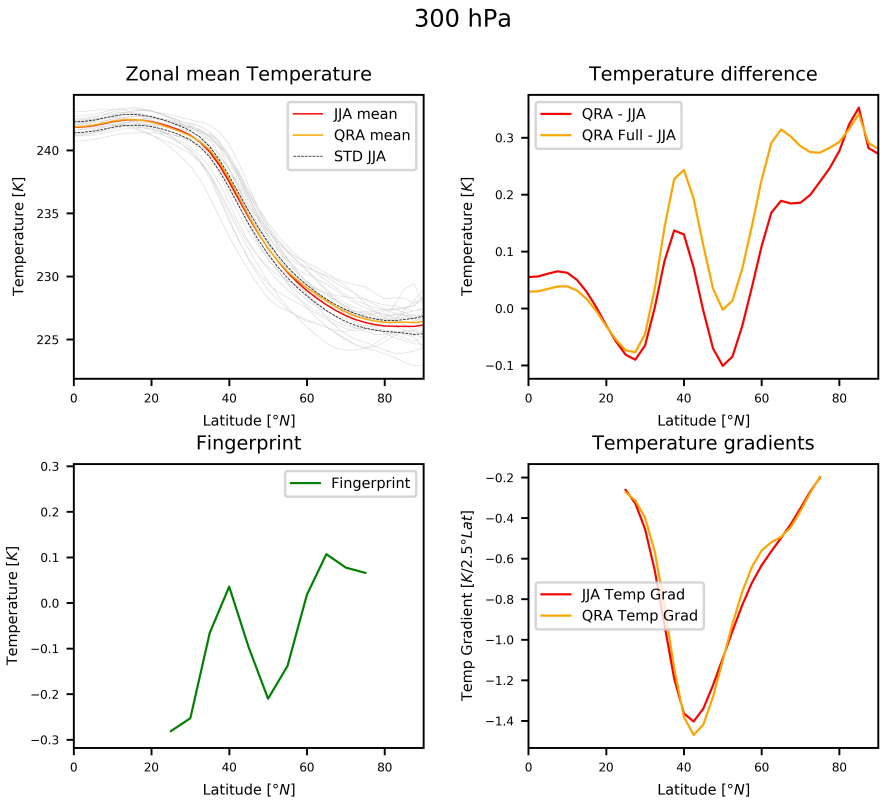

Figure 5.8: Same as Fig. 5.7, but with 300 hPa temperature data.

5.2 Vertical structure

To get a fuller picture of a possible climate change influence on QRA, the fingerprint as defined by M17 was calculated for various pressure levels and is presented in Fig. 5.9. The only areas where the fingerprint has positive values are in the range of 55°N to 75°N for the lower atmosphere (1000 hPa to 925 hPa) and upper atmosphere (650 hPa to 250 hPa). In between those two layers, the fingerprint has a pronounced minimum at low and high latitudes, and is negative across all latitudes. Therefore it can be split into three components, the low and high altitude fingerprint, and the middle altitude fingerprint. Investigating how these project onto yearly zonal mean JJA means temperature fields in their respective height is of great importance in determining possible climate change induced changes in occurrence of QRA events, giving possible insight into the tug of war. This is done in Sections 5.3.2 and 5.3.3.

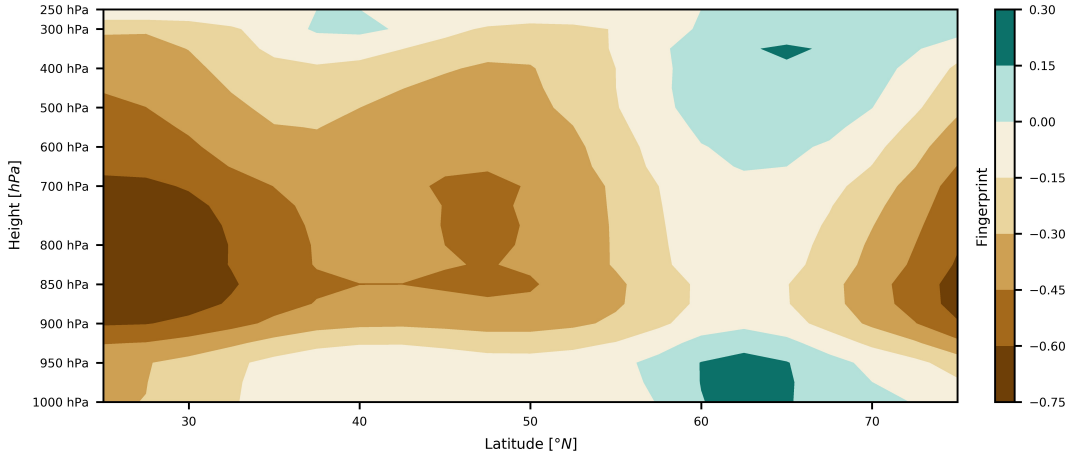

Figure 5.9: Vertical structure of the fingerprint.

5.3 Regressions

5.3.1 Observational data

Following M17, the fingerprint as calculated here was projected onto yearly GISTEMP and HadCrut4 temperature anomalies, using linear regression. The evolution of the regression coefficients for both datasets are shown in Fig. 5.10, for monthly and JJA means. Unlike the results shown in Fig. 5 of M17, no positive trends were detected here. On the contrary, with the Fingerprint of Fig. 5.7 from this work, only negative trends are detected (see Tab. 5.1). A positive trend in the regression coefficients would mean a more pronounced correlation between yearly zonal mean JJA mean temperature fields and the fingerprint, therefore implying an increase in number of QRA events. However, the trends found here are very small and can be considered insignificant when compared to the internal variability and magnitude of the regression coefficients. Extending the period for the calculation of the trends until 2020, results in even smaller trends (dark blue line in Fig. 5.10, -0.002 for JJA means of both datasets). Fluctuations of the fingerprint are very strong, changing from negative to positive values often within a period of a few years. This is indicative of a strong dependence of the proposed relationship between the fingerprint and JJA climatology on internal variability.

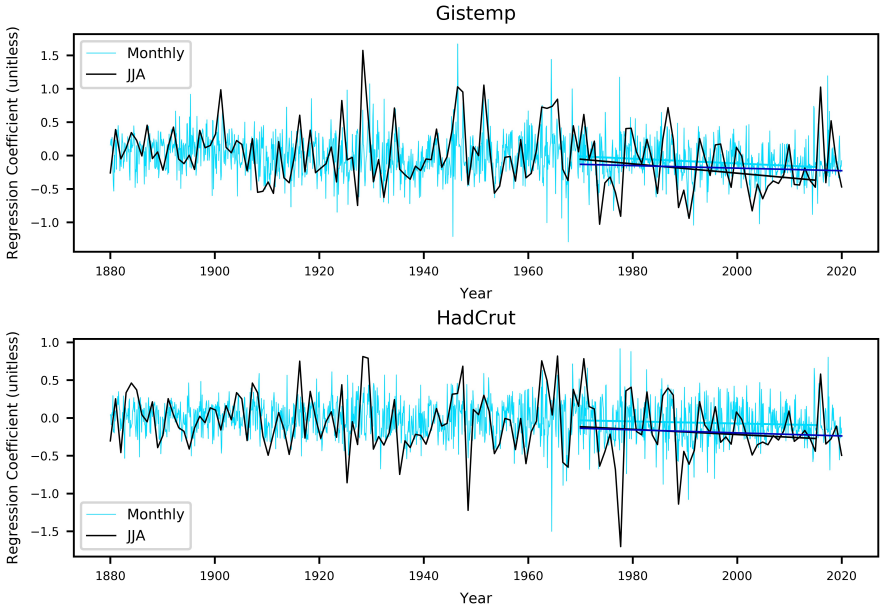

Figure 5.10: Trends of regression coefficient for projection of fingerprint onto yearly zonal mean JJA surface temperature field using GISTEMP and HadCrut4 monthly and JJA mean datasets. Cyan and black trends were calculated from 1970 to 2015, as in M17. Dark blue trends were calculated from 1970 to 2020.

Table 5.1: Trends of regression coefficients from 1970 to 2015, for monthly and JJA means of GISTEMP and HadCrut4 datasets. Units are (change of regression coefficient)/month for monthly data and (change of regression coefficient)/JJA for JJA mean data.

	Monthly	JJA
GISTEMP	-0.004	-0.007
HadCrut4	-0.001	-0.003

5.3.2 ERA-Interim

The same analysis as in the previous Section has also been done for ERA-Interim data, for surface temperature fields and additionally various pressure levels. Fig. 5.11 shows the historical evolution of the correlation coefficient for levels 1000 hPa, 900 hPa, 700 hPa and 300 hPa. All of the trends are positive, however strongest for levels 700 hPa and 1000 hPa, which is in contradiction with the observational datasets from the previous Section, where surface trends were negative (Fig. 5.10). Again, the yearly fluctuations of the regression coefficient are very strong. Fig. 5.12 shows the regression coefficients of the trends for all available pressure levels. They are positive across all levels, however vary significantly in magnitude. Interesting to note are the maxima at 1000 hPa and 500 hPa, as well as the minima at 975 hPa and 300 hPa.

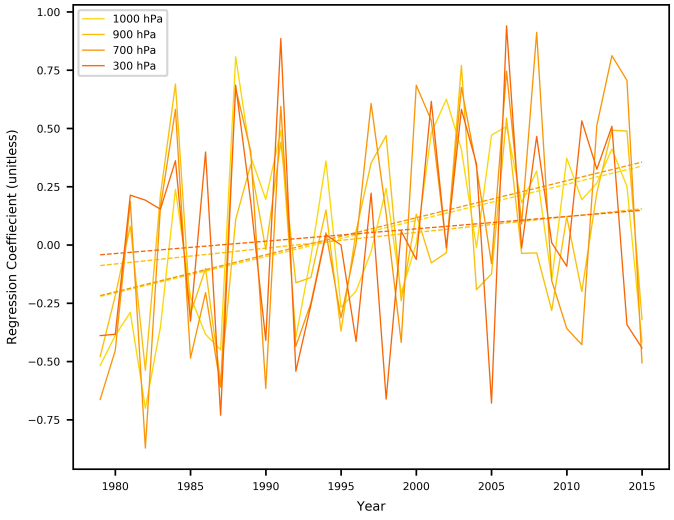

Figure 5.11: Historical evolution and trends of regression coefficient from fingerprint projection onto yearly zonal mean JJA temperature fields for selected pressure levels using ERA-Interim data.

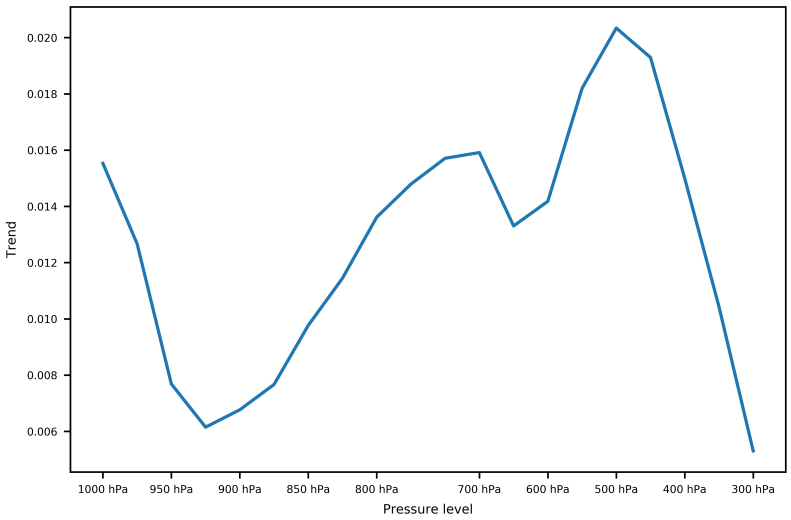

Figure 5.12: Trends of the regression coefficient time series across all available pressure levels using ERA-Interim data.

5.3.3 CMIP5

For comparison, the fingerprints for various levels were also projected onto historical temperature fields of CMIP5 models HadGem2-AO, CNRM-CM5 and IPSL-CM5A-LR. For the 300 hPa level the results are shown in Fig. 5.13. No historical 300 hPa data was available for the HadGem-2AO, therefore only CNRM-CM5 and IPSL-CM5A-LR models are shown. In contrast to the ERA-Interim dataset, the IPSL-CM5A-LR model projections for this level show a negative trend from 1985 to 2005. However, the regression coefficients are overall smaller than those of the ERA-Interim projections, and exhibit large yearly fluctuations, sometimes changing the correlation from negative values to positive values within less than five years. This behaviour for these two models is present for any pressure level and scenario. Looking at the CNRM-CM5 model, the regression coefficients are even smaller (in the range of ≈ 0.025) and show no significant trend, which is the same for all pressure levels and scenarios.

For the 1000 hPa historical evolution of the regression coefficients (Fig. 5.14) none of the three models show significant trends, and are as well smaller compared to ERA-Interim and observational datasets, with the CNRM-CM5 projection again showing barely any correlation.

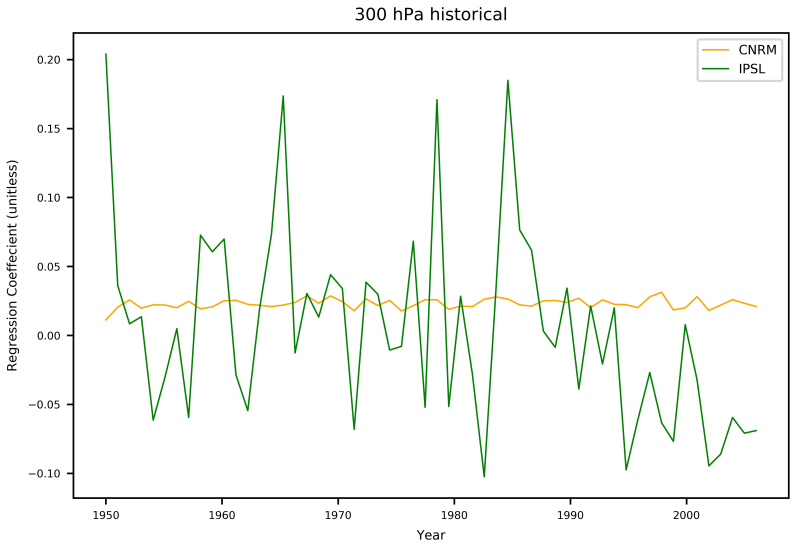

Figure 5.13: Historical evolution of regression coefficient from fingerprint projection onto yearly zonal mean 300 hPa JJA temperature fields using CMIP5 models CNMR-CM5 and IPSL-CMA5-LR.

For the RCP8.5 scenario and 300 hPa temperature data, the results of the projection are shown in Fig. 5.15. HadGem2-AO and IPSL-CM5A-LR model data shows a negative trend for the regression coefficients in the second half of the 21st century, that seems to stagnate towards the end of the century. The regression coefficients are in the range of -0.6 to 0.4 for these two models, and very small again for the CNRM-CM5 model data, which shows no trend.
Contrary to the 300 hPa level, the projections for the 1000 hPa level show a positive trend throughout the 21st century for models HadGem2-AO and IPSL-CM5A-LR, whereas the regression on CNRM-CM5 data produces again very small coefficients, with no significant trend. However, the large fluctuations for the HadGem2-AO and IPSL-CM5A-LR model data should be noted. These fluctuations are strongest for the HadGem2-AO model for all considered pressure levels. On the 1000 hPa level they become less towards the end of the century, whereas for the 300 hPa it is the opposite. This could be related to the tug of war, where a strengthening temperature gradient in the upper troposphere due to tropical warming (i.e. 300 hPa level) introduces a dependency on the internal variability, whereas for the 1000 hPa the opposite is the case (weakening temperature gradient due to AA).

Historical and projected climatologies for the three selected models are shown in Figs. 5.17 and 5.18, for 300 hPa and 1000 hPa levels, respectively. For both levels, the historical and future projections from the CNRM-CM5 model do not correspond well with the other two models under consideration. This is especially the case for the 1000 hPa data, the historical temperature climatology being hotter than the RCP8.5 projections from the HadGem2-AO and IPSL-

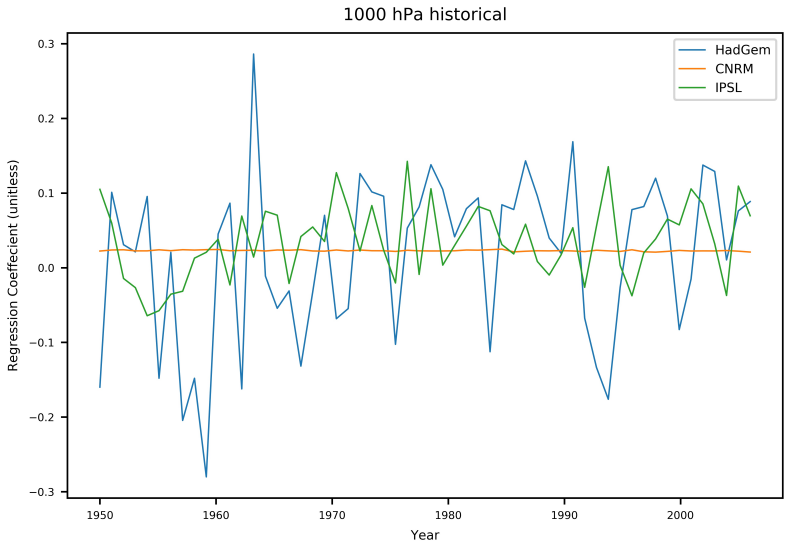

Figure 5.14: Same as Fig. 5.13 but for 1000 hPa temperature data.

CM5A-LR models, except in the 0°N to 15°N and 60°N to 75°N latitude ranges. Comparing the historical climatologies to ERA-Interim derived climatologies, suggests that CNRM-CM5 data corresponds best for 1000 hPa level and IPSL-CM5A-LR for 300 hPa.

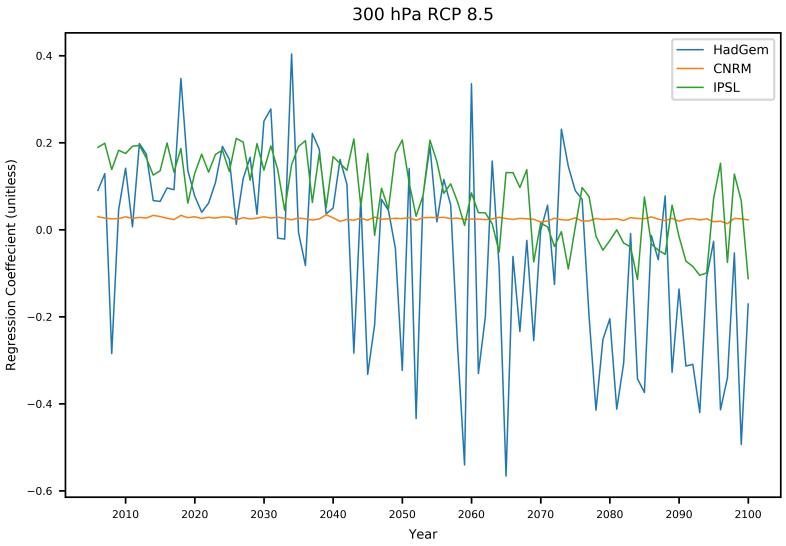

Figure 5.15: RCP 8.5 evolution of regression coefficient from fingerprint projection onto yearly zonal mean 300 hPa JJA temperature fields using CMIP5 models HadGem2-AO, CNMR-CM5 and IPSL-CM5A-LR.

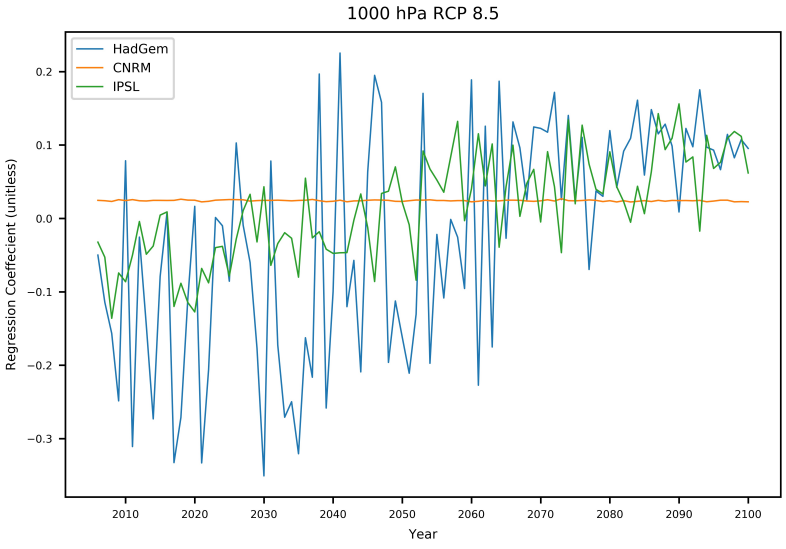

Figure 5.16: Same as Fig. 5.15 but with 1000 hPa temperature data.

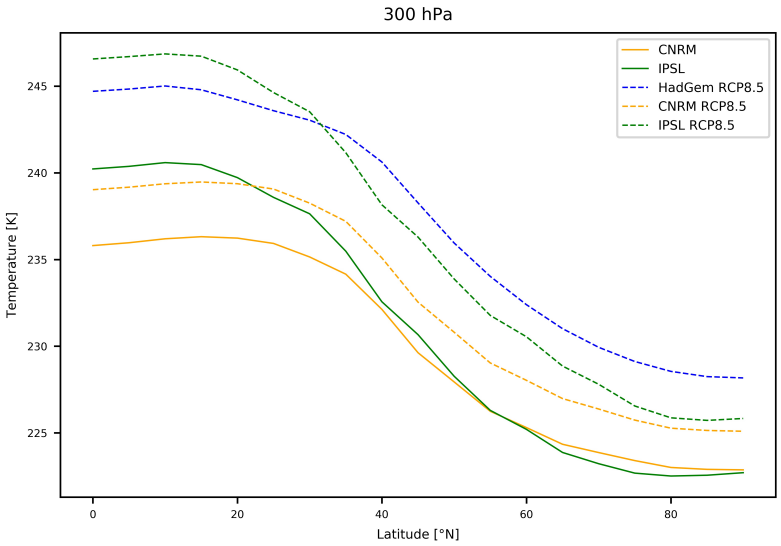

Figure 5.17: 300 hPa zonal mean JJA temperature climatologies for historical period (1850-2006) and RCP 8.5 (2006-2100) for CMIP5 models HadGem2AO, CNMR and IPSL.

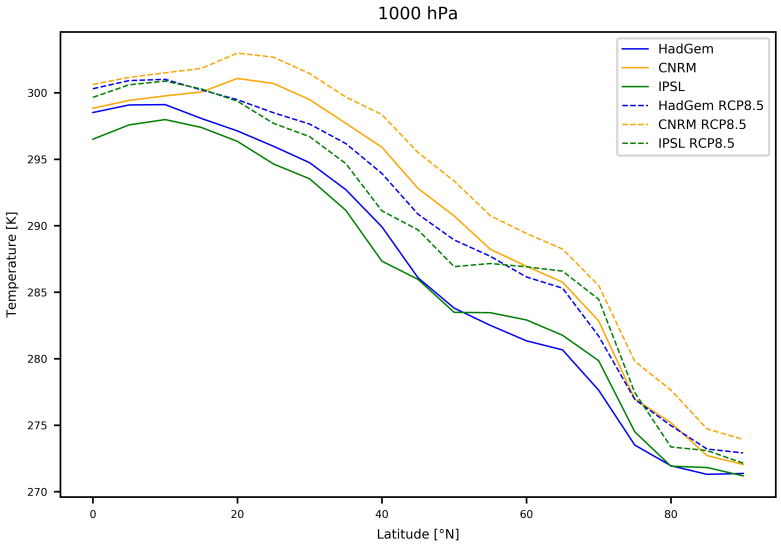

Figure 5.18: Same as Fig. 5.17 but for 1000 hPa temperature data.

6 Thermal wind

The meridional surface temperature gradient is weakening due to AA, whereas the upper atmosphere meridional temperature gradient is strengthening, due to tropical warming. It has been argued that this weakening/strengthening has an impact on the thermal component of the jet stream. It is not clear however, whether the changes in the upper or lower atmosphere dominate. The following analysis is meant to give insight into the applicability of the thermal wind equation to different atmospheric layers and their respective virtual temperature gradients. This is done by calculating the thermal wind and calculating the Pearson correlation with the actual wind shear, using temperature data within a restricted domain (25° N to 70° N and -40° E to 40° E) from ERA-Interim from 1979 to 2015, for June, July and August of each individual year.

The calculation of the zonal thermal wind caused by an atmospheric layer between an upper and lower boundary is done using the following equation (Lynch & Cassano 2006)

$$u = -\frac{R_{air}}{f} \ln \frac{p_l}{p_u} \frac{dT}{dy} \tag{6.1}$$

where $R_{air} = 287\ m^2 s^{-2} K^{-1}$ is the specific gas constant for air, $f = 10^{-4}\ s^{-1}$ is the Coriolis parameter, p_l is the lower and p_u the upper boundary in hPa, and $\frac{dT}{dy}$ is the zonal mean meridional virtual temperature gradient of the mean of the layer between p_l and p_u. The virtual temperature was calculated by using the following equation (Pedlosky & Robertson 1988):

$$T_v = T(1 + 0.61 * w) \tag{6.2}$$

where T is the temperature given by ERA-Interim data, and $w = \frac{q}{1-q}$ is the mixing ratio calculated from the specific humidity q from ERA-Interim data. This is an approximation to the original formula, however differences were found to be sufficiently small (in the order of 10^{-3}) to use this approximation.
Eq. 6.1 was applied to all possible atmospheric layers between 1000 hPa and 300 hPa. The 1000 hPa wind field was then added to the calculated thermal wind of the different layers and the result was then correlated with the wind shear, i.e. the difference between 1000 hPa and 300 hPa zonal wind field.

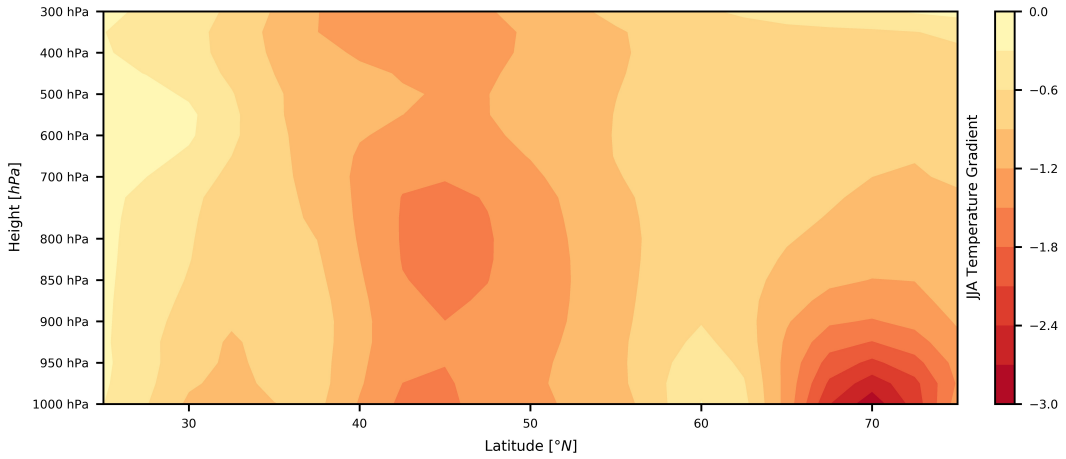

Figure 6.1: Vertical structure of the zonal mean JJA meridional temperature gradient averaged from 1979 to 2015.

Fig. 6.1 shows the climatological (1979 to 2015) mean of the meridional virtual temperature gradient for available pressure levels from 1000 hPa to 300 hPa. In the climatological mean there is a recognisable vertical structure. However, on smaller timescales such as monthly or seasonal means this vertical structure can be disrupted, affecting the contribution of certain layers to the thermal jet. This can be nicely seen in Figs. 6.2, 6.3 and 6.4 which used monthly mean data

from June 1990, July 1990 and July 2010 for the calculation of the thermal wind, respectively. The analysis of these three specific months was chosen to be displayed because they demonstrate a variety in relative importance of different atmospheric layers and because of their high correlation.
For June 1990 (Fig. 6.2) it is evident, that, the thicker the layer, the lower the correlation, whereas for thinner layers their vertical displacement does not change the correlation. This is due to a relative error of the equation that grows with the layer thickness that is used for the calculation. This is a common problem, throughout other years as well. The blue area (correlation ≤ 0.15) indicates that no calculation of a difference between two levels was possible (i.e. there is only one possible layer with thickness 700 hPa, namely the one from 1000 hPa to 300 hPa). All the calculated correlations are bigger than 0.15. Looking at Fig. 6.3, which uses data from July 1990, the dominating layers seem to be overall thicker, as well as situated slightly above the ground. The decreasing correlation with increasing layer thickness is the strongest from the three examples shown here for July 2010 data. This raises the question whether the relative error that comes from the equation is associated with certain atmospheric, such as QRA favouring, conditions.

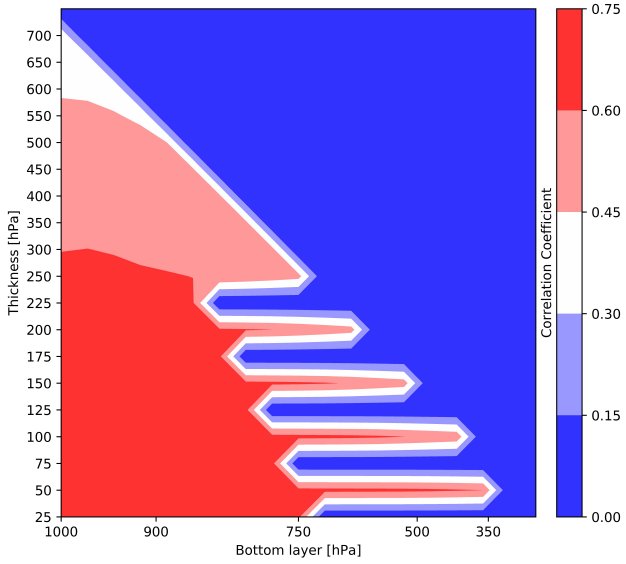

Figure 6.2: Correlation coefficients between calculated thermal wind of all possible layers and thicknesses between 1000 hPa and 300 hPa, and the actual wind shear, using temperature monthly mean data from June 1990. The x-axis is showing the bottom layer that was used for calculation and the y-axis is showing the thickness of the layer. Moving along the x-axis corresponds to changing layers with the same thickness, whereas moving vertically changes only the thickness and the bottom layer stays at the same height.

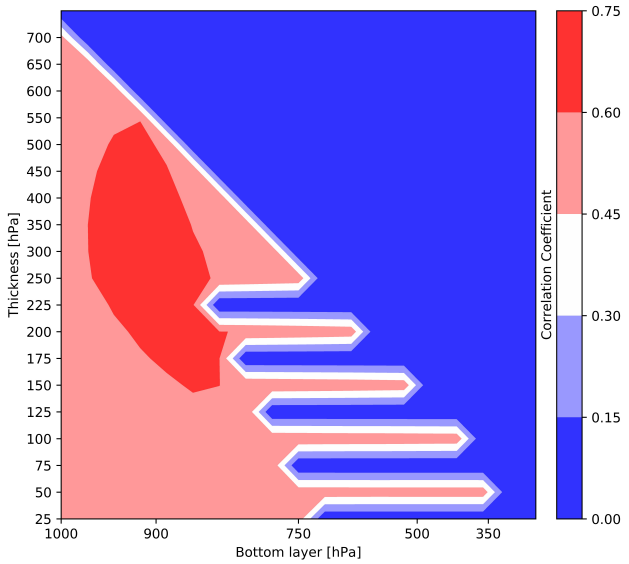

Figure 6.3: Same as Fig. 6.2 but for July 1990.

Across all years from 1979 to 2015 however, no relationship between either high or low correlation coefficients and wavenumber 7 QRA events has been found. The three examples given in this section clearly demonstrate the dependence of the thermal wind equation on which layers and layer thicknesses are used for the calculation, as well as display the internal variability of this dependence on monthly (see i.e. Figs. 6.2 and 6.3) and yearly (see i.e. Figs. 6.3 and 6.4) timescales. No trend for the emergence of a preferable layer for the thermal wind calculation has been found, that could've potentially given insight into the tug of war. This might be due to the recent emergence of AA or due to the high internal variability of the mean temperature over the selected area.

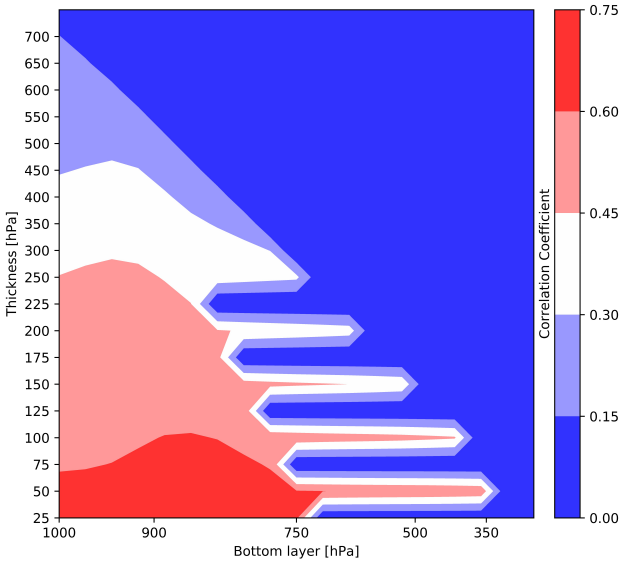

Figure 6.4: Same as Fig. 6.2 but for July 2010.

7 Synthesis, Conclusions and Outlook

7.1 Synthesis

There are a lot of possibilities through which climate change can have an impact on mid-latitude weather extremes such as heat waves. From purely thermodynamical considerations, heat waves are expected to become more frequent and intense. Influences on mid-latitude dynamics and therefore heat wave mechanisms are more complex and can be either directly or indirectly (through AA linkages) responsible for changes on blocking dynamics, the jet stream, the storm track or planetary waves. Possible changes in heat wave frequency and intensity have been investigated on the basis of the QRA theory by Mann et al. (2017, 2018). Their interest in this research question was spurred by the idea that a weakening meridional temperature gradient reduces the thermal part of the jet stream, leading to a slower and more meandering jet, which is more favourable for QRA. However, an important issue is the tug of war between a reducing meridional temperature gradient in the lower and an increasing gradient in the upper troposphere. Currently it is not yet understood whether the jet is expected to strengthen or weaken due to the changing temperature gradients.
One key assumption of Mann et al. (2017) is that the relationship between the fingerprint and the climatological zonal mean surface temperature stays the same. This is a strong assumption to make, considering the fact that the meridional temperature gradient is expected to change. This gradient is not only subject of change due to AA, but also due to changes in mid-latitude dynamics, which are a lot harder to predict. Furthermore, not only the surface temperature gradient is expected to change, but also the gradients from the layers higher up in the atmosphere. Therefore a more complete picture of the atmosphere during QRA events (or a vertically extended fingerprint) is needed, to account for all possible influences on the meridional temperature gradients in different atmospheric layers.

7.2 Summary

Analysis of internal variability of zonal and JJA mean temperature data of all available pressure levels from ERA-Interim showed that the temperature anomalies during QRA events lie within one standard deviation of JJA climatologies for most latitudes and pressure levels. For levels 300 hPa and 1000 hPa this is shown in Figs. 5.5 and 5.6. The calculated surface fingerprint presented here (Fig. 5.7) is approximately only half in amplitude of the one calculated by Mann et al. (2017), however very similar in shape. For the 300 hPa level the fingerprint is shown in Fig. 5.8. It should be noted that across all levels, averaging over total QRA days results in a greater magnitude of the fingerprint than averaging over QRA episodes and then again. Fig. 5.9

shows the vertical structure of the fingerprint.
Fingerprints for all levels have been projected onto yearly JJA zonal mean temperature profiles for ERA-Interim (Figs. 5.11 and 5.12), observational (GISTEMP and HadCrut4 in Fig. 5.10) as well as CMIP5 (HadGem2-AO, CNRM-CM5 and IPSL-CM5A-LR in Figs. 5.13 to 5.16) data. Trends of the regression coefficient for the observational datasets are negative from 1979 to 2015, which contradicts the results from M17. For ERA-Interim data the trends are positive for all available pressure levels, although the correlation coefficients are smaller than for the observational datasets. For the CMIP5 models the results strongly depend on the three randomly selected models and the correlation coefficients are smaller than for the observational and ERA-Interim datasets, for historical as well as future projections. The CNRM-CM5 model data results in a very small correlation coefficient (≤ 0.05), due to a poor representation of yearly JJA means (see climatologies in Figs. 5.17 and 5.18). No significant trends are detected for the 1000 hPa historical simulations from 1979 to 2015. For the 300 hPa simulations the IPSL-CM5A-LR model shows a trend from 1985 to 2006. For RCP8.5 scenarios, the HadGem2-AO and IPSL-CM5A-LR model data show a positive trend over the 21st century, whereas the model data from CNRM-CM5 again produces very small regression coefficients and no trend. For the 300 hPa level, HadGem2-AO and IPSL-CM5A-LR show a negative trend over the 21st century, data from the CNRM-CM5 model projects again very poorly.
The layers contributing most to a high correlation between calculated thermal wind and observed 1000 hPa to 300 hPa wind shear can vary significantly on yearly and even monthly timescales as demonstrated by Figs. 6.2, 6.3 and 6.4. There was no trend found for the emergence of a preferred layer for a high correlation.

7.3 Conclusions and Potential Research

The same QRA detection scheme that was developed by Kornhuber et al. (2016) was implemented in the research for this thesis. It was not possible to reproduce the findings by Kornhuber et al. (2016), although a lot of effort was put into this first step. The reasons for the different outcome of the implementation still remain unclear.
It was found that the QRA climatology of the meridional temperature gradient lies within the range of the standard deviation of the JJA climatology, therefore raising the question whether the signal is of sufficient magnitude. However, the fingerprint which is calculated from the difference between the two climatologies is found to be only half in amplitude of the one calculated M17, therefore raising the need to be careful with the interpretation of the results of this thesis. Furthermore, the fingerprint seems to have a defined vertical structure that can be used for further research regarding the tug of war of the changing temperature gradients, as well as projections on the circulation of the mid-latitudes, since the phenomena of QRA is influenced by various layers of the atmosphere.
Again, the role of internal variability should be emphasized. This can also be seen in Figs. 3 and 5 of M17, where individual model simulations (Fig. 3) and observational datasets (Fig 5.) show large variation of the regression coefficient time series. The signal to noise ratio of the multi model mean to the individual ensemble members is very low, therefore suggesting that models project the fingerprint very differently, which can be also seen in Figs. 5.13 to 5.16. Future

research could therefore focus on selected models that represented specific storylines (low/high arctic/tropical amplification) to evaluate the respective contribution of these effects to a change of the QRA mechanism and give insight into the outcome of the tug of war of upper and lower changing temperature gradients. Modelling studies could be conducted to further extent the research from Section 6, to see if a trend for a dominant atmospheric layer contributing to the thermal part of the jet stream emerges in the future.
While there is some evidence for QRA to be responsible for devastating heatwaves and associated impacts like droughts and crop losses, the possible influence of climate change on this mechanism is still a highly debatable topic, owing to the complexity and uncertainty of the changes in dynamical drivers the QRA.

Bibliography

Austin, J. F. (1980), 'The blocking of middle latitude westerly winds by planetary waves', *Quarterly Journal of the Royal Meteorological Society* **106**(448), 327–350.
URL: *https://rmets.onlinelibrary.wiley.com/doi/abs/10.1002/qj.49710644807*

Barnes, E. A. & Polvani, L. (2013), 'Response of the Midlatitude Jets, and of Their Variability, to Increased Greenhouse Gases in the CMIP5 Models', *Journal of Climate* **26**(18), 7117–7135.
URL: *https://doi.org/10.1175/JCLI-D-12-00536.1*

Barnes, E. A. & Screen, J. A. (2015), 'The impact of Arctic warming on the midlatitude jetstream: Can it? Has it? Will it?', *WIREs Climate Change* **6**(3), 277–286.
URL: *https://onlinelibrary.wiley.com/doi/abs/10.1002/wcc.337*

Barriopedro, D., Sousa, P. M., Trigo, R. M., García-Herrera, R. & Ramos, A. M. (2020), 'The Exceptional Iberian Heatwave of Summer 2018', *Bulletin of the American Meteorological Society* **101**(1), S29–S34.
URL: *https://doi.org/10.1175/BAMS-D-19-0159.1*

Bastos, A., Ciais, P., Friedlingstein, P., Sitch, S., Pongratz, J., Fan, L., Wigneron, J. P., Weber, U., Reichstein, M., Fu, Z., Anthoni, P., Arneth, A., Haverd, V., Jain, A. K., Joetzjer, E., Knauer, J., Lienert, S., Loughran, T., McGuire, P. C., Tian, H., Viovy, N. & Zaehle, S. (2020), 'Direct and seasonal legacy effects of the 2018 heat wave and drought on European ecosystem productivity', *Science Advances* **6**(24).
URL: *https://advances.sciencemag.org/content/6/24/eaba2724*

Black, E., Blackburn, M., Harrison, G., Hoskins, B. & Methven, J. (2004), 'Factors contributing to the summer 2003 European heatwave', *Weather* **59**(8), 217–223.
URL: *https://rmets.onlinelibrary.wiley.com/doi/abs/10.1256/wea.74.04*

Ceppi, P. & Hartmann, D. (2015), 'Connections Between Clouds, Radiation, and Midlatitude Dynamics: a Review', *Current Climate Change Reports* **1**.

Cohen, J., Screen, J., Furtado, J., Barlow, M., Whittleston, D., Coumou, D., Francis, J., Dethloff, K., Entekhabi, D., Overland, J. & Jones, J. (2014), 'Recent Arctic amplification and extreme mid-latitude weather', *Nature Geoscience* **7**, 627–637.

Cohen, J., Zhang, X., Francis, J., Jung, T., Kwok, R., Overland, J., Ballinger, T., Bhatt, U., Chen, H., Coumou, D., Feldstein, S., Gu, H., Handorf, D., Henderson, G., Ionita, M., Kretschmer, M., Laliberté, F., Lee, S., Linderholm, H. & Yoon, J.-H. (2019), 'Divergent consensuses on Arctic amplification influence on midlatitude severe winter weather', *Nature Climate Change* **10**, 1–10.

Coumou, D., Di Capua, G., Vavrus, S., Wang, L. & Wang, S.-Y. (2018), 'The influence of Arctic amplification on mid-latitude summer circulation', *Nature Communications* **9**.

Coumou, D. & Rahmstorf, S. (2012), 'A decade of weather extremes', *Nature Climate Change* **2**, 491–496.

De Bono, A., Giuliani, G., Kluser, S. & Peduzzi, P. (2004), 'Impacts of summer 2003 heat wave in Europe'.

de Vries, H., Woollings, T., Anstey, J., Haarsma, R. & Hazeleger, W. (2013), 'Atmospheric blocking and its relation to jet changes in future climate', *Climate Dynamics* pp. –.

Dee, D. P., Uppala, S. M., Simmons, A. J., Berrisford, P., Poli, P., Kobayashi, S., Andrae, U., Balmaseda, M. A., Balsamo, G., Bauer, P., Bechtold, P., Beljaars, A. C. M., van de Berg, L., Bidlot, J., Bormann, N., Delsol, C., Dragani, R., Fuentes, M., Geer, A. J., Haimberger, L., Healy, S. B., Hersbach, H., Hólm, E. V., Isaksen, L., Kållberg, P., Köhler, M., Matricardi, M., McNally, A. P., Monge-Sanz, B. M., Morcrette, J.-J., Park, B.-K., Peubey, C., de Rosnay, P., Tavolato, C., Thépaut, J.-N. & Vitart, F. (2011), 'The ERA-Interim reanalysis: configuration and performance of the data assimilation system', *Quarterly Journal of the Royal Meteorological Society* **137**(656), 553–597.
URL: *https://rmets.onlinelibrary.wiley.com/doi/abs/10.1002/qj.828*

Dufresne, J.-L., Foujols, M.-A., Denvil, S., Caubel, A., Marti, O., Aumont, O., Balkanski, Y., Bekki, S., Bellenger, H., Benshila, R., Bony, S., Bopp, L., Braconnot, P., Brockmann, P., Cadule, P., Cheruy, F., Codron, F., Cozic, A., Cugnet, D. & Vuichard, N. (2013), 'Climate change projections using the IPSL-CM5 earth system model: from CMIP3 to CMIP5', *Climate Dynamics* **40**, 2123–2165.

Fischer, E. M., Seneviratne, S. I., Lüthi, D. & Schär, C. (2007), 'Contribution of land-atmosphere coupling to recent European summer heat waves', *Geophysical Research Letters* **34**(6), 491–496.

Gabriel, A. & Peters, D. (2008), 'A Diagnostic Study of Different Types of Rossby Wave Breaking Events in the Northern Extratropics', *Journal of the Meteorological Society of Japan. Ser. II* **86**(5), 613–631.

Goosse, H., Barriat, P.-Y., Lefebvre, W., Loutre, M.-F. & Zunz, V. (2009), *Introduction to climate dynamics and climate modeling*.

Graversen, R. G. (2006), 'Do Changes in the Midlatitude Circulation Have Any Impact on the Arctic Surface Air Temperature Trend?', *Journal of Climate* **19**(20), 5422–5438.
URL: *https://doi.org/10.1175/JCLI3906.1*

Grumm, R. H. (2011), 'The Central European and Russian Heat Event of July–August 2010', *Bulletin of American Meteorological Society* .

Hoskins, B. J. & Karoly, D. (1981), 'Steady Linear Respons of a Spherical Atmosphere to Thermal and Orographic Forcing', *American Meteorological Society* **38**, 1179–1196.

Hoskins, B. J., Simmons, A. J. & Andrews, D. (1977), 'Energy dispersion in a barotropic atmosphere', *Quarterly J. R. Met. Soc* **103**, 553–567.

Kalnay, E., Kanamitsu, M., Kistler, R., Collins, W., Deaven, D., Gandin, L., Iredell, M., Saha, S., White, G., Woollen, J., Zhu, Y., Chelliah, M., Ebisuzaki, W., Higgins, W., Janowiak, J., Mo, K. C., Ropelewski, C., Wang, J., Leetmaa, A., Reynolds, R., Jenne, R. & Joseph, D. (1996), 'The NCEP/NCAR 40-Year Reanalysis Project', *Bulletin of the American Meteorological Society* **77**(3), 437–472.
URL: *https://doi.org/10.1175/1520-0477(1996)077<0437:TNYRP>2.0.CO;2*

Koppe, C., Kovats, S., Jendritzky, G. & Menne, B. (2004), 'Heat-waves: risks and responses', *Health and Global Environmental Change Series* **2**.

Kornhuber, K., Osprey, S., Coumou, D., Petri, S., Petoukhov, V., Rahmstorf, S. & Gray, L. (2019), 'Extreme weather events in early summer 2018 connected by a recurrent hemispheric wave-7 pattern', *Environmental Research Letters* **14**(5), 054002.

Kornhuber, K., Petoukhov, V., Petri, S., Rahmstorf, S. & Coumou, D. (2016), 'Evidence for wave resonance as a key mechanism for generating high-amplitude quasi-stationary waves in boreal summer', *Climate Dynamics* **49**.

Lenssen, N. J. L., Schmidt, G. A., Hansen, J. E., Menne, M. J., Persin, A., Ruedy, R. & Zyss, D. (2019), 'Improvements in the GISTEMP Uncertainty Model', *Journal of Geophysical Research: Atmospheres* **124**(12), 6307–6326.
URL: *https://agupubs.onlinelibrary.wiley.com/doi/abs/10.1029/2018JD029522*

Luterbacher, J., Dietrich, D., Xoplaki, E., Grosjean, M. & Wanner, H. (2004), 'European Seasonal and Annual Temperature Variability, Trends, and Extremes Since 1500', *Science* **303**(5663), 1499–1503.
URL: *https://science.sciencemag.org/content/303/5663/1499*

Lynch, A. & Cassano, J. (2006), *Applied Atmospheric Dynamics*.

Mann, M. E., Rahmstorf, S., Kornhuber, K., Steinman, B. A., Miller, S. K. & Coumou, D. (2017), 'Influence of Anthropogenic Climate Change on Planetary Wave Resonance and Extreme Weather Events', *Scientific Reports* **7**.

Mann, M. E., Rahmstorf, S., Kornhuber, K., Steinman, B. A., Miller, S. K., Petri, S. & Coumou, D. (2018), 'Projected changes in persistent extreme summer weather events: The role of quasi-resonant amplification', *Science Advances* **4**.

Martin, T., Bellouin, N., Collins, W., Culverwell, I., Halloran, P., Hardiman, S., Hinton, T., Jones, C., McDonald, R., McLaren, A., O'Connor, F., Roberts, M., Rodriguez, J., Woodward, S., Best, M., Brooks, M., Brown, A., Butchart, N., Dearden, C. & Wiltshire, A. (2011), 'The HadGEM2 family of Met Office Unified Model Climate configurations', *Geoscientific Model Development* **4**, 723–757.

Masato, G., Hoskins, B. J. & Woollings, T. J. (2012), 'Wave-breaking characteristics of midlatitude blocking', *Quarterly Journal of the Royal Meteorological Society* **138**(666), 1285–1296.
URL: *https://rmets.onlinelibrary.wiley.com/doi/abs/10.1002/qj.990*

Mbengue, C. & Schneider, T. (2013), 'Storm Track Shifts under Climate Change: What Can Be Learned from Large-Scale Dry Dynamics', *Journal of Climate* **26**(24), 9923–9930.
URL: *https://doi.org/10.1175/JCLI-D-13-00404.1*

Mbengue, C. & Schneider, T. (2016), 'Storm-Track Shifts under Climate Change: Toward a Mechanistic Understanding Using Baroclinic Mean Available Potential Energy', *Journal of the Atmospheric Sciences* **74**(1), 93–110.
URL: *https://doi.org/10.1175/JAS-D-15-0267.1*

Morice, C. P., Kennedy, J. J., Rayner, N. A. & Jones, P. D. (2012), 'Quantifying uncertainties in global and regional temperature change using an ensemble of observational estimates: The HadCRUT4 data set', *Journal of Geophysical Research: Atmospheres* **117**(D8).
URL: *https://agupubs.onlinelibrary.wiley.com/doi/abs/10.1029/2011JD017187*

Mullen, S. L. (1987), 'Transient Eddy Forcing of Blocking Flows', *Journal of the Atmospheric Sciences* **44**(1), 3–22.
URL: *https://doi.org/10.1175/1520-0469(1987)044<0003:TEFOBF>2.0.CO;2*

Nakamura, H., Nakamura, M. & Anderson, J. L. (1997), 'The Role of High- and Low-Frequency Dynamics in Blocking Formation', *Monthly Weather Review* **125**(9), 2074–2093.
URL: *https://doi.org/10.1175/1520-0493(1997)125<2074:TROHAL>2.0.CO;2*

Pedlosky, J. & Robertson, J. S. (1988), 'Geophysical Fluid Dynamics by Joseph Pedlosky', *The Journal of the Acoustical Society of America* **83**(3), 1207–1207.
URL: *https://doi.org/10.1121/1.396028*

Peterson, T. C., Stott, P. A. & Herring, S. (2012), 'Explaining Extreme Events of 2011 from a Climate Perspective', *Bulletin of the American Meteorological Society* **93**(7), 1041–1067.
URL: *https://doi.org/10.1175/BAMS-D-12-00021.1*

Petoukhov, V., Rahmstorf, S., Petri, S. & Schellnhuber, H. J. (2013), 'Quasiresonant amplification of planetary waves and recent Northern Hemisphere weather extremes', *Proceedings of the National Academy of Sciences* **110**(14), 5336–5341.
URL: *https://www.pnas.org/content/110/14/5336*

Phillips, N. A. (1973), *Principles of Large Scale Numerical Weather Prediction*, Springer Netherlands, pp. 1–96.

Rahmstorf, S. & Coumou, D. (2011), 'Increase of extreme events in a warming world', *Proceedings of the National Academy of Sciences* **108**(44), 17905–17909.
URL: *https://www.pnas.org/content/108/44/17905*

Renwick, J. A. & Revell, M. J. (1999), 'Blocking over the South Pacific and Rossby Wave Propagation', *Monthly Weather Review* **127**(10), 2233–2247.
URL: *https://doi.org/10.1175/1520-0493(1999)127<2233:BOTSPA>2.0.CO;2*

Rex, D. F. (1950), 'Blocking Action in the Middle Troposphere and its Effect upon Regional Climate', *Tellus* **2**(3), 196–211.
URL: *https://doi.org/10.3402/tellusa.v2i3.8546*

Schneider, T., Bischoff, T. & Płotka, H. (2015), 'Physics of Changes in Synoptic Midlatitude Temperature Variability', *Journal of Climate* **28**(6), 2312–2331.
URL: *https://doi.org/10.1175/JCLI-D-14-00632.1*

Schär, C., Vidale, P., Lüthi, D., Frei, C., Häberli, C., Liniger, M. & Appenzeller, C. (2004), '2004: The role of increasing temperature variability in European summer heatwaves', *Nature* **427**, 332–6.

Screen, J. A., Deser, C. & Simmonds, I. (2012), 'Local and remote controls on observed Arctic warming', *Geophysical Research Letters* **39**(10).
URL: *https://agupubs.onlinelibrary.wiley.com/doi/abs/10.1029/2012GL051598*

Screen, J. & Simmonds, I. (2010), 'The Central Role of Diminishing Sea Ice in Recent Arctic Temperature Amplification', *Nature* **464**, 1334–7.

Shaw, T., Baldwin, M., Barnes, E., Caballero, R., Garfinkel, C., Hwang, Y.-T., Li, C., O'Gorman, P., Rivière, G., Simpson, I. & Voigt, A. (2016), 'Storm track processes and the opposing influences of climate change', *Nature Geoscience* **9**.

Shutts, G. J. (1983), 'The propagation of eddies in diffluent jetstreams: Eddy vorticity forcing of 'blocking' flow fields', *Quarterly Journal of the Royal Meteorological Society* **109**(462), 737–761.
URL: *https://rmets.onlinelibrary.wiley.com/doi/abs/10.1002/qj.49710946204*

Vogel, M. M., Zscheischler, J., Wartenburger, R., Dee, D. & Seneviratne, S. I. (2019), 'Concurrent 2018 Hot Extremes Across Northern Hemisphere Due to Human-Induced Climate Change', *Earth's Future* **7**(7), 692–703.
URL: *https://agupubs.onlinelibrary.wiley.com/doi/abs/10.1029/2019EF001189*

Voldoire, A., Sanchez-Gomez, E., Mélia, D., Decharme, B., Cassou, C., Senesi, S., Valcke, S., Beau, I., Alias, A., Chevallier, M., Déqué, M., Deshayes, J., Douville, H., Fernandez, E., Madec, G., Maisonnave, E., Moine, M.-P., Planton, S., Saint-Martin, D. & Chauvin, F. (2013), 'The CNRM-CM5.1 global climate model: description and basic evaluation', *Climate Dynamics* **40**.

Wilks, D. (2006), *Statistical Methods in the Atmosphere Science*, Vol. 38.

Wirth, V. (2020), 'Waveguidability of idealized midlatitude jets and the limitations of ray tracing theory', *Weather and Climate Dynamics* **1**(1), 111–125.
URL: *https://wcd.copernicus.org/articles/1/111/2020/*

Woollings, T., Barriopedro, D., Methven, J., Son, S.-W., Martius, O., Harvey, B., Sillmann, J., Lupo, A. & Seneviratne, S. (2018), 'Blocking and its Response to Climate Change', *Current Climate Change Reports* **4**, 1–14.

Woollings, T., Gregory, J., Pinto, J., Reyers, M. & Brayshaw, D. (2012), 'Response of the North Atlantic storm track to climate change shaped by ocean– atmosphere coupling', *Nature Geoscience* .

Yamazaki, A. & Itoh, H. (2013), 'Vortex–Vortex Interactions for the Maintenance of Blocking. Part I: The Selective Absorption Mechanism and a Case Study', *Journal of the Atmospheric Sciences* **70**(3), 725–742.
URL: *https://doi.org/10.1175/JAS-D-11-0295.1*

Yang, L., Sun, G., Zhi, L. & Zhao, J. (2018), 'Negative soil moisture-precipitation feedback in dry and wet regions', *Scientific Reports* **8**.

Yin, J. H. (2005), 'A consistent poleward shift of the storm tracks in simulations of 21st century climate', *Geophysical Research Letters* **32**(18).
URL: *https://agupubs.onlinelibrary.wiley.com/doi/abs/10.1029/2005GL023684*